UNIVERSITY OF ZURICH

Angular Analysis of Z-Events at LHCb

FACULTY OF SCIENCE

DEPARTMENT OF PHYSICS

BACHELOR THESIS

OF

LUKAS RUOSCH

Prof. Dr. Nicola Serra

Dr. Katharina Müller

Dr. Albert Puig

June 21, 2018

Abstract

A measurement of the muon angular distribution in Z boson decays in the Drell-Yan process is presented. The Z bosons are produced in pp collisions at $\sqrt{s} = 8$ TeV and are decaying to $\mu^+\mu^-$. The results are based on data corresponding to a luminosity of 2 fb^{-1} collected by the LHCb detector at the CERN LHC in 2012. The study of the angular coefficients $A_{i=0,\ldots,7}$ provides comprehensive information about the underlying QCD production mechanism of the Z boson. A measurement of the coefficients as a function of the transverse momentum is provided and compared to theoretical predictions and previous measurements from ATLAS and CMS.

Acknowledgement

Contents

1 Theory

1.1 Standard Model

The Standard Model (SM) of particle physics describes the fundamental particles and the interactions between them [1]. It provides a successful description of experimental findings in many different regimes and represents one of the triumphs of modern physics [2]. The particles in the SM can be split into two groups according to their spin: fermions with half integer spin and bosons with full integer spin. In the SM, bosons are the force-carriers and are exchanged between fermions and/or bosons to transmit a force. There are three forces in the SM: the electromagnetic force, the weak and the strong force. Each particle has a corresponding anti-particle, which has the same mass, but opposite charge quantum numbers. The fermions consist of two groups of elementary particles, the quarks and the leptons, which are divided into three generations with two members each, called flavors. The muon (μ^-) is a lepton of the second generation and basically a copy of the electron, but with a mass of 106 MeV/c^2 it is about 200 times heavier. Its antiparticle is the μ^+. A proton consists of three "valence" quarks, but also contains a sea of virtual gluons, which are the mediators of the strong force, quarks and antiquarks. The Z boson is the electrically neutral mediator of the weak force. Unlike the photon and the gluon it has a mass, and is very heavy with 91.2 GeV/c^2.

1.2 Process

At leading order (LO), the Z boson, that is decaying to two muons, is produced in a hadron collision through the Drell-Yan annihilation of an incoming quark-antiquark pair of two protons [3]. The Feynman diagram for this process is shown in Fig. 1.1. The production rate for this process is extremely large and allows for precise differential Z boson cross section measurements [4]. In addition to the on-shell Z boson production, there are contributions from Drell-Yan γ^* production and γ^*Z interference.

Figure 1.1: LO Feynman diagram for the production of a Z boson decaying to two muons through the Drell-Yan process in a collision of two protons [3].

Two examples of next-to-leading order (NLO) Feynman diagrams for the production of Z bosons decaying to two muons are shown in Fig. 1.2.
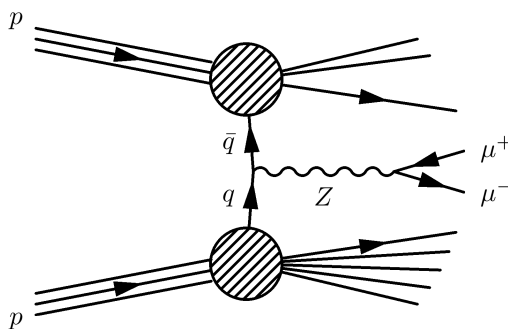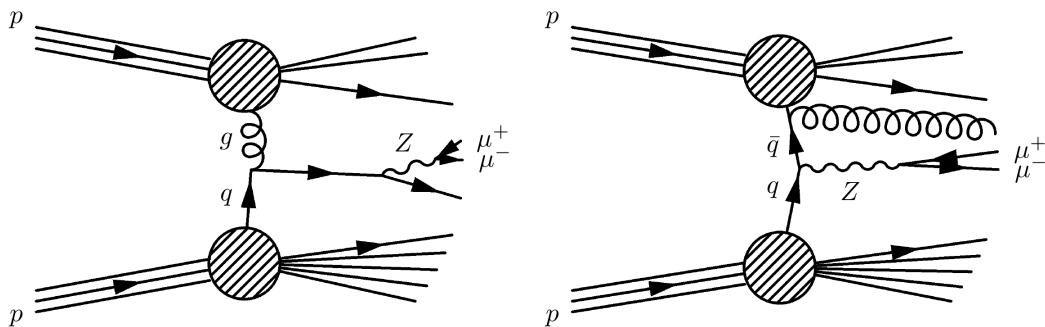
Figure 1.2: NLO Feynman diagrams for the production of a Z boson decaying to two muons through the Drell-Yan process in a collision of two protons. Quark gluon scattering with a resulting quark jet in the final state (left), Drell-Yan process with gluon radiation producing a gluon jet (right) [3].

1.3   Angles definition

The direction of the trajectories of the two muons in the lab frame is defined by two angles in the coordinate system of the detector, which is described in Section 2.1. The polar angle θ is the angle between the momentum of the particle and the z axis. In terms of the momentum parameters of the particle in the lab frame, it is defined by Eq. (1). The azimuthal angle ϕ is the angle measured with respect to the x axis and defined by Eq. (2).

$$\theta = \arccos\left(\frac{p_z}{|\vec{p}|}\right) \tag{1}$$

$$\phi = \arctan\left(\frac{p_y}{p_x}\right) \tag{2}$$

However the angles of interest for this analysis are the ones in the rest frame of the decaying Z boson. They are labeled with an asterisk (*) throughout this thesis and are defined by the momentum parameters of the particle in the Z rest frame (Eqs. (3) and (4)).

$$\theta^* = \arccos\left(\frac{p_z^*}{|\vec{p}^*|}\right) \tag{3}$$

$$\phi^* = \arctan\left(\frac{p_y^*}{p_x^*}\right) \tag{4}$$

A commonly used spatial coordinate describing the angle of a particle relative to the beam axis is the pseudorapidity η. It is strictly a function of the angle θ of a particle (Eq. (5)), but can be re-written in terms of the momentum parameters.

$$\eta = -\ln[\tan\left(\frac{\theta}{2}\right)] = \frac{1}{2}\ln\left[\frac{|\mathbf{p}| + p_z}{|\mathbf{p}| - p_z}\right] \tag{5}$$

Fig. 1.3 shows the pseudorapidity η as a function of the polar angle θ on the left and η for certain values of θ on the right.
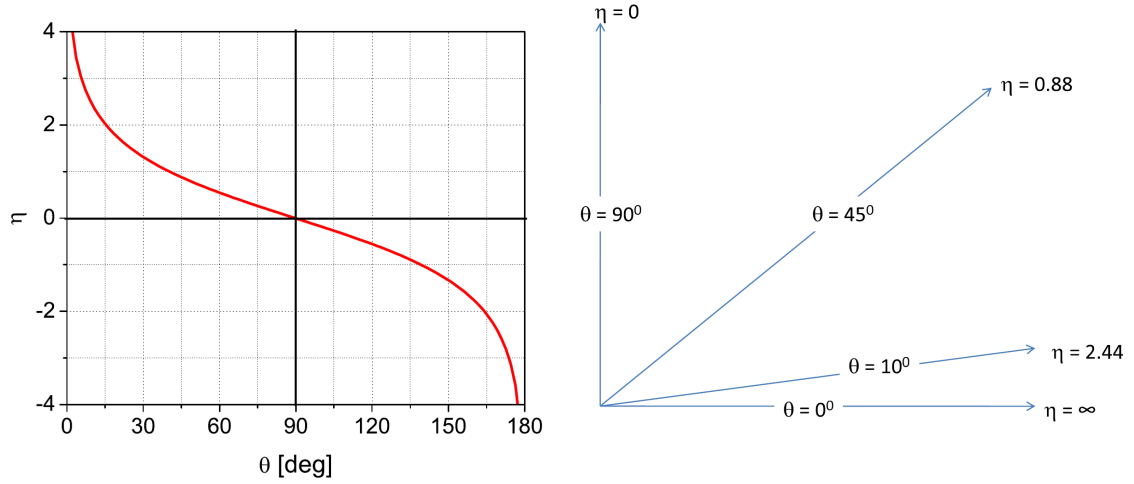
Figure 1.3: Pseudorapidity η as a function of the polar angle θ (left), η for certain values of θ (right) [5].

1.4 Angular dependence

When the Z boson is produced with no transverse momentum and parity is conserved, the leading order Drell-Yan process, $q\bar{q} \to Z \to \mu^+\mu^-$, predicts a $1 + \cos^2\theta^*$ distribution for the leptons [6] in the rest frame of the gauge boson. Z bosons produced with transverse momentum provide a convenient reference plane for studying the angular distributions of the leptons. By studying this angular distribution of the final-state leptons, tests of the QCD dynamics for the Z boson production can be performed [4]. The QCD dynamics of this process can be expressed in terms of eight frame dependent angular coefficients $A_{i=0,\dots,7}$, which also depend on the invariant mass (m^Z), the transverse momentum (p_T^Z) and the pseudorapidity (η^Z) of the Z boson and describe the production of the intermediate gauge boson. The reference frame of choice is the Collins-Soper (CS) frame shown in Fig. 1.4.
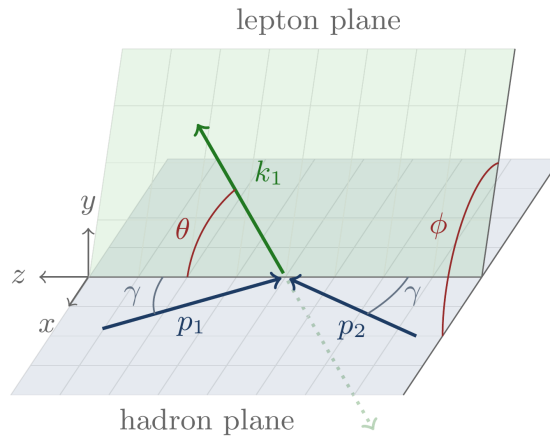

Figure 1.4: The definition of the angles in the Collins-Soper frame. Proton momenta (p_1 and p_1) lie in the hadron plane, leptons (k_1) in the lepton plane. The x axis is collinear to p_T^Z and the y axis is orthogonal to the hadronic event plane and chosen to complete a right-handed Cartesian coordinate system [4].

The CS reference frame [7] is a Z rest frame where the z axis lies in the plane of the incoming protons (hadron plane) and bisects the angle between the momentum (p_1) of one proton and the negative momentum (p_2) of the other proton. This results in an angle γ between each proton and the z axis, because for $p_T^Z \neq 0$, p_1 and p_2 are not parallel in the CS frame. The x direction is collinear to p_T^Z and the y axis is orthogonal to the hadronic event plane and chosen to complete a right-handed Cartesian coordinate system. The angles (in Fig. 1.4 denoted θ and ϕ without asterisk) of the outgoing lepton momentum (k_1) are measured with respect to the z axis and x axis, respectively [8]. The transformation of the muon momenta from the lab frame to the CS frame is done in three steps [9]:

- a rotation around the z axis by an angle α so that p_T^Z is oriented along x, where

$$\alpha = \arccos\left(\frac{p_x^Z}{p_T^Z}\right); \tag{6}$$

- a boost along z so that the Z boson is at rest with respect to the z axis;

- a boost along the new x axis so that Z is completely at rest.

For the boost to the Z rest frame, the four-momenta of the muons are transformed in the following way, using contravariant notation [5]:

$$p'^{\rho}(\mu) = \Lambda^{\rho}{}_{\sigma}(Z)\, p^{\sigma}(\mu) \tag{7}$$

$$\text{where } p^{\sigma}(\mu) = \begin{pmatrix} E/c \\ p_x \\ p_y \\ p_z \end{pmatrix}, \; p'^{\rho}(\mu) = \begin{pmatrix} E^*/c \\ p_x^* \\ p_y^* \\ p_z^* \end{pmatrix},$$

with the asterisk (*) denoting the variable to be in the reference frame of the Z boson,

$$\text{and } \Lambda^{\rho}{}_{\sigma}(Z) = \begin{pmatrix} \gamma & -\gamma\beta_x & -\gamma\beta_y & -\gamma\beta_z \\ -\gamma\beta_x & 1 + (\gamma-1)\frac{\beta_x^2}{\beta^2} & (\gamma-1)\frac{\beta_x\beta_y}{\beta^2} & (\gamma-1)\frac{\beta_x\beta_z}{\beta^2} \\ -\gamma\beta_y & (\gamma-1)\frac{\beta_y\beta_x}{\beta^2} & 1 + (\gamma-1)\frac{\beta_y^2}{\beta^2} & (\gamma-1)\frac{\beta_y\beta_z}{\beta^2} \\ -\gamma\beta_z & (\gamma-1)\frac{\beta_z\beta_x}{\beta^2} & (\gamma-1)\frac{\beta_z\beta_y}{\beta^2} & 1 + (\gamma-1)\frac{\beta_z^2}{\beta^2} \end{pmatrix}$$

The boost $\Lambda^{\rho}{}_{\sigma}(Z)$ is defined by the kinematics of the Z boson of each event:

$$\gamma = \frac{E_Z}{m_Z c^2}, \text{ with } m_Z = \sqrt{E_Z^2 - \vec{p}_Z^2}, \; \beta = \frac{|\vec{p}_Z|c}{E_Z}, \; \beta_i = \frac{p_{iZ}c}{E_Z}, \; i = \{x, y, z\}$$

The general structure of the muon angular distribution is then given by Eq. (8), where θ^* and ϕ^* are the polar and azimuthal angles of the muons in the CS frame. The parameters A_0, A_1 and A_2 are related to the polarization of the Z boson, whilst A_3 and A_4 are also sensitive to the vector and axial vector (V-A) structure of the couplings of the muons. All angular coefficients vanish for p_T^Z approaching zero, except for A_4, which is the electroweak parity violation term [10]. The angular coefficients A_0 and A_2 satisfy an important relation known as the Lam-Tung relation, $A_0 - A_2 = 0$. This relation can be shown to hold up to

10

$\mathcal{O}(\alpha_s)$. At leading order, it is a direct consequence of the spin-$\frac{1}{2}$ nature of the quarks, and is further preserved at $\mathcal{O}(\alpha_s)$ due to the vector-coupling of the spin-1 gluon to quarks.

$$
\begin{aligned}
\frac{\mathrm{d}^2\sigma}{\mathrm{d}\cos\theta^*\,\mathrm{d}\phi^*} \propto \Big\{ &(1+\cos^2\theta^*) + \frac{1}{2}\,A_0\,(1-3\cos^2\theta^*) \\
&+ A_1\,\sin(2\theta^*)\cos\phi^* + \frac{1}{2}\,A_2\,\sin^2\theta^*\cos(2\phi^*) \\
&+ A_3\,\sin\theta^*\cos\phi^* + A_4\,\cos\theta^* + A_5\,\sin^2\theta^*\sin(2\phi^*) \\
&+ A_6\,\sin(2\theta^*)\sin\phi^* + A_7\,\sin\theta^*\sin\phi^* \Big\},
\end{aligned}
\tag{8}
$$

To extract the full set of coefficients $(A_{i=0,...,7})$, both angles must be fitted simultaneously. By integrating over $\cos\theta^*$ and ϕ^*, the information about A_1 and A_6 is lost. Integrating Eq. (8) over $\cos\theta^*$ yields:

$$
\frac{\mathrm{d}\sigma}{\mathrm{d}\phi^*} \propto \left\{ 1 + \frac{1}{4}\,A_2\,\cos(2\phi^*) + \frac{3\pi}{16}\,A_3\,\cos\phi^* + \frac{1}{2}\,A_5\,\sin(2\phi^*) + \frac{3\pi}{16}\,A_7\,\sin\phi^* \right\},
\tag{9}
$$

and integrating Eq. (8) over ϕ^* yields:

$$
\frac{\mathrm{d}\sigma}{\mathrm{d}\cos\theta^*} \propto \left\{ (1+\cos^2\theta^*) + \frac{1}{2}\,A_0\,(1-3\cos^2\theta^*) + A_4\,\cos\theta^* \right\}.
\tag{10}
$$

2   Detector

2.1   Setup

The LHCb detector [11, 15] is a high-precision single-arm spectrometer at the Large Hadron Collider (LHC) at CERN. It is designed to study CP violation and rare decays of beauty and charm hadrons, but also serves as a general purpose detector in the forward region. It has a polar angular coverage from approximately 15 mrad to 270 mrad, which corresponds to a pseudorapidity acceptance of about $2 < \eta < 5$. The acceptance is the fraction of events that is visible in the detector due to its geometry. The layout of the LHCb spectrometer is shown in Fig. 2.1. A right-handed coordinate system is defined such that z is along the beam axis, y vertical and x horizontal. Where appropriate, cylindrical coordinates (r, ϕ, z) are used. The detector consists of the Vertex Locator (VELO) surrounding the pp interaction region, four planar tracking stations (TT, T1-T3), a dipole magnet, two Ring Imaging Cherenkov detectors (RICH 1&2), a calorimeter system consisting of a Scintillating Pad Detector (SPD), an electromagnetic calorimeter with pre-shower (ECAL, PS), a hadronic calorimeter (HCAL), and muon chambers (M1-M5).

2.2   Tracking system

The tracking system consists of the vertex locator (VELO) and the four planar tracking stations (TT, T1-T3) [11, 3]. The VELO is situated around the interaction region inside a vacuum tank and contains 42 silicon micro-strip sensors arranged along the beam axis
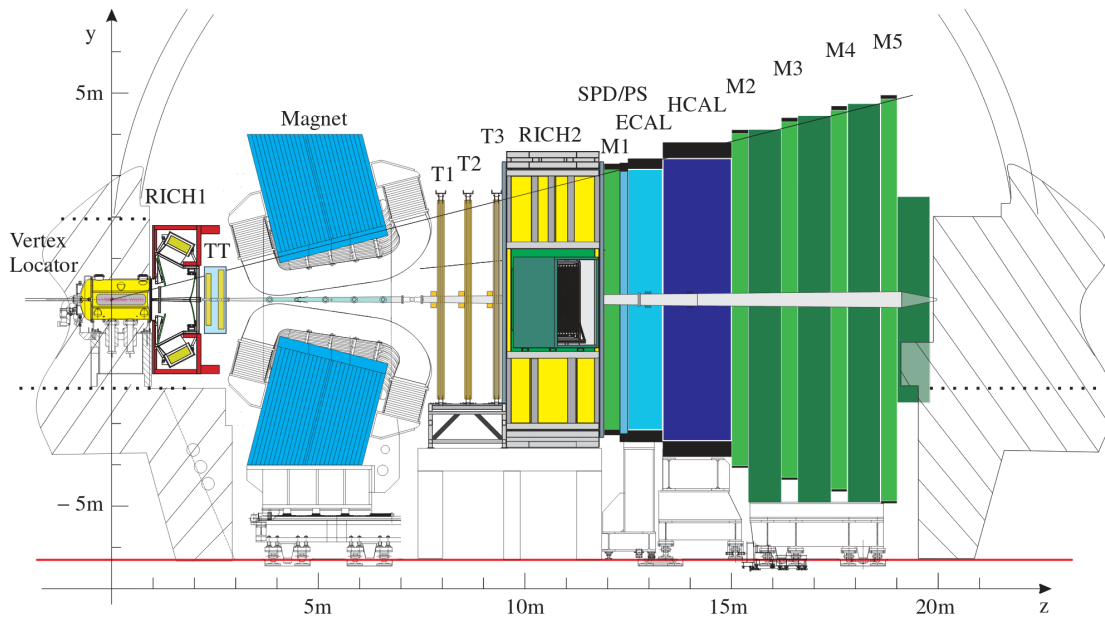
Figure 2.1: LHCb detector layout, showing the Vertex Locator (VELO), the dipole magnet, the two RICH detectors, the four tracking stations TT and T1-T3, the Scintillating Pad Detector (SPD), the Electromagnetic (ECAL) and Hadronic (HCAL) Calorimeters, and the five muon stations M1-M5. It also shows the direction of the y and z coordinate axes; the direction of the x axis goes into the plane [12].

(Fig. 2.2), each providing a measurement of the r and ϕ coordinates of primary and secondary vertices with high precision. The Tracker Turicensis (TT) is located upstream and the three tracking stations (T1-T3) downstream of the magnet. The latter are divided into inner (IT) and outer tracker (OT). Due to the high flux in the region around the beam pipe, silicon microstrip sensors are used for the TT and the IT of T1-T3. The OT of T1-T3 are equipped with straw-tube detectors.

2.3 Track reconstruction

The trajectories of charged particles traversing the tracking system are reconstructed from hits in the VELO, TT, IT and OT. The most important tracks for physics analyses in general are long tracks. They traverse the full tracking system and have hits in the VELO, in the T stations and optionally in TT. As they traverse the full magnetic field, their momentum is determined with the highest precision.

The tracking efficiency [11] is defined as the probability that the trajectory of a charged particle that has passed through the full tracking system is reconstructed. It does not account for interactions with the material, decays in flight and particles that fly outside of the detector acceptance. The average efficiency is above 96%, but decreases for a larger number of tracks per event. Only for events with more than 200 tracks it is less than 96%. Fake tracks also have an effect on the efficiency. A reconstructed track is considered as fake, if it does not correspond to the trajectory of a genuine charged particle [11]. The LHCb detector is designed to minimize the material of the tracking detectors and thus provides a high efficiency for track reconstruction. However, the smaller number of tracking stations results in more fake tracks. The fraction of fake tracks in events is typically around 6.5%, increasing to about 20% for large multiplicity events [13].
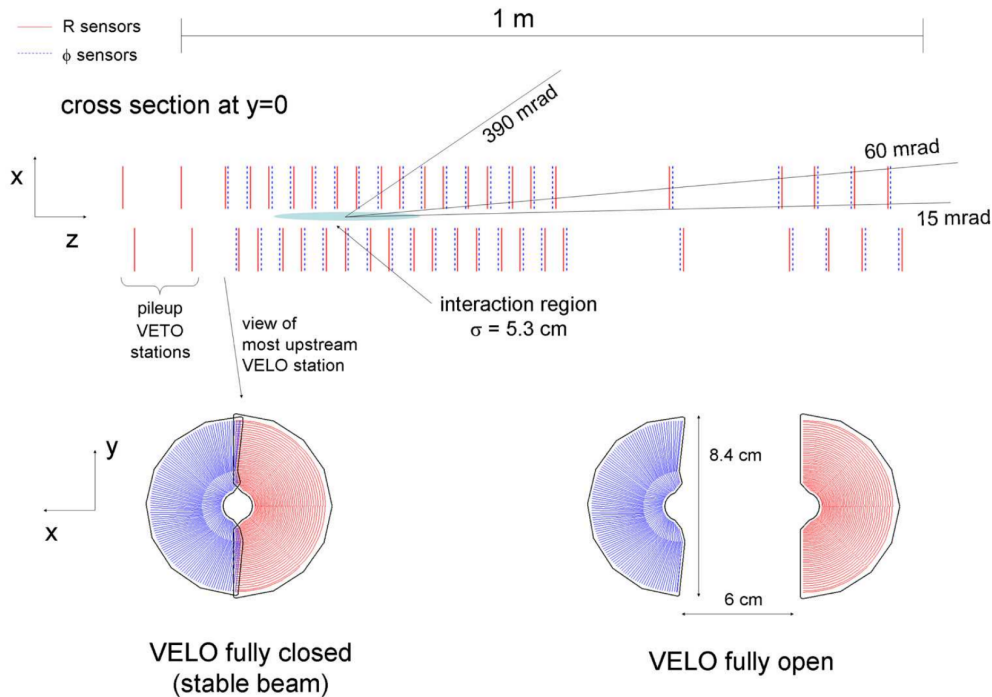
Figure 2.2: Top: Layout of the 42 silicon modules of the VELO along the beam axis in the $x - z$ plane with the two pile-up VETO stations on the left. Bottom: Setup of a closed (left) and open (right) VELO module in the $x - y$ plane [14].

2.4 Detector resolution

For the analysis of this thesis the resolutions of the primary vertex (PV), the momentum and the mass are the most relevant.

The PV resolution [11] is measured by comparing two independent measurements of the vertex position in the same event. This is achieved by randomly splitting the set of tracks in an event into two and reconstructing the PVs in both sets. The width of the distribution of the difference of the vertex positions is used to extract the vertex resolution. A vertex consists of a minimum of 5 to around 150 tracks and the more tracks a vertex is made of, the smaller is the PV resolution. Fig. 2.3 shows the PV resolution in the x and y direction as a function of the number of tracks. A PV with 25 tracks has a resolution of 13 μm in x and y and 71 μm in z.

The momentum resolution [11], δ_p/p, is extracted for long tracks using $J/\psi \rightarrow \mu^+\mu^-$ decays. Fig. 2.3 shows the relative momentum resolution as a function of the momentum p. The momentum resolution is about 0.5% for particles below 20 GeV/c rising to about 0.9% for particles around 100 GeV/c.

The relative mass resolution, σ_m/m, is for lower masses up to about 10 GeV/c^2 about 0.5% and in the region of the mass of the Z boson (91.2 GeV/c^2) about 2% [11]. The mass resolution for the dimuon resonance of the Z boson is 1727 ± 64 MeV/c^2, which is extracted from a single Gaussian function with power-law tail, convolved with a Breit-Wigner function of a fixed width. The uncertainty is statistical only.
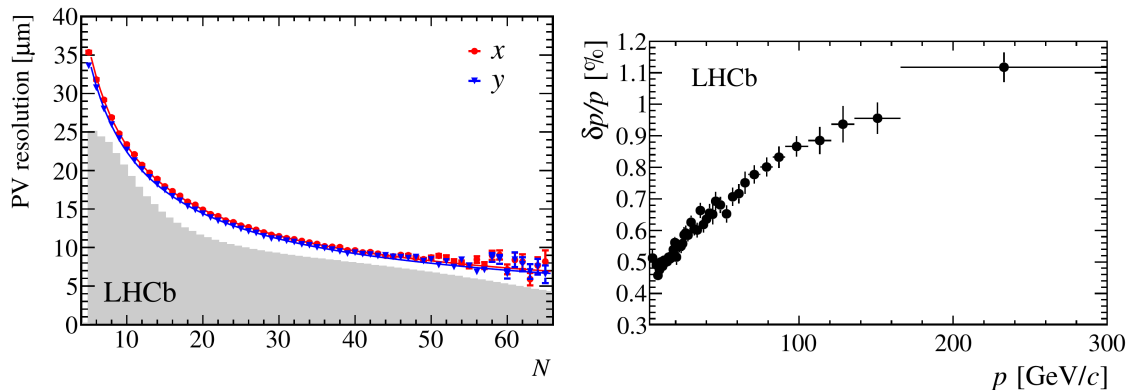
Figure 2.3: Primary vertex resolution (left), for events with one reconstructed primary vertex in the x (red) and y (blue) direction, as a function of the number of tracks. The histogram (grey) shows the distribution of the number of tracks per reconstructed primary vertex. Relative momentum resolution as a function of the momentum (right) [11].

2.5   Magnet

A warm dipole magnet with an integrated field of about 4 Tm is used to bend charged particles and hence allow the measurement of their momenta [11, 3]. The coil consists of fifteen layers of pure hollow aluminium conductors with a channel for water cooling inside. The polarity of the magnet is regularly reversed during data acquisition to minimise systematic effects of the measurements. To reach its design sensitivity in CP violation measurements, LHCb aims to control such detection asymmetries to a precision of 10^{-3} or better. The field of the spectrometer magnet also has an impact on the trajectory of the LHC beams. Three dipole magnets are used to compensate for this effect.

2.6   Particle identification

Several detector systems are used to identify different particle types; Cherenkov detectors, a calorimeter system and a muon detection system [11, 3].

Two Ring Imaging Cherenkov detectors (RICH1 and RICH2) are used for distinguishing charged hadrons using Cherenkov light. Located between the VELO and TT is RICH1, which covers the low momentum particle range and the full LHCb acceptance. The emitted Cherenkov light is reflected onto an array of Pixel Hybrid Photon Detectors (HPDs) at the top and bottom of RICH1, outside the acceptance. In the HPDs the photoelectrons are accelerated onto a pixel sensor, which provides a position measurement. RICH2 is situated further downstream between the three tracking stations (T1-T3) and the first muon station (M1), covering the high momentum range and only a reduced angular acceptance. The mirrors of RICH2 are situated to the left and right of the beam pipe.

The calorimeter system serves several purposes and is composed of four parts; the scintillating pad detector (SPD), the pre-shower detector (PS), the electromagnetic calorimeter (ECAL) and the hadronic calorimeter (HCAL). They provide the identification of electrons, photons and hadrons as well as the measurement of their energies and positions, and selects candidates with high transverse energy for the first trigger level (L0).

The muon detection system provides muon identification and contributes to the L0 trigger of the experiment. It is composed of five stations; M1 situated between RICH2

and the electromagnetic calorimeter (ECAL) and M2-M5 downstream of the hadronic calorimeter (HCAL). They are of rectangular shape and predominantly equipped with Multi Wire Proportional Chambers (MWPC), except in region with the highest rate (M1), where triple Gas Electron Multiplier (GEM) detectors are used.

2.7 Trigger

The bunch crossing frequency at the interaction point of LHCb is 40 MHz [3, 14, ?]. The frequency with interactions visible[1] by the spectrometer is about 10 MHz, which has to be reduced by the trigger to about 5 kHz, to allow the data to be written to tape. The architecture of the LHCb trigger consists of two levels, illustrated in Fig. 2.4; the first level trigger (L0) and the High Level Trigger (HLT).
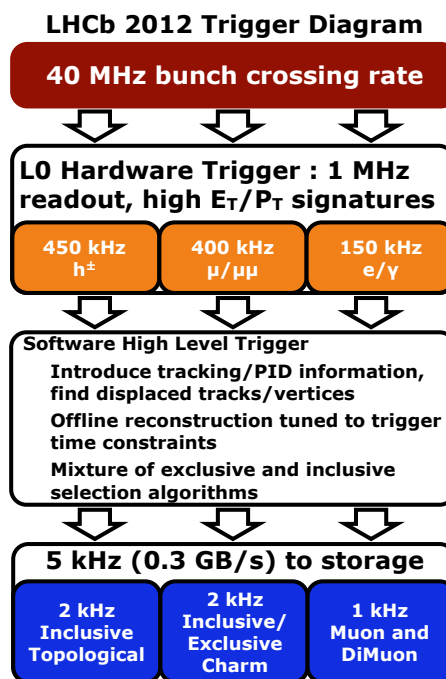

Figure 2.4: Scheme of the LHCb trigger in 2012 [15].

L0 is implemented using custom made electronics and uses input from the pile-up veto system included in the VELO, shown in Fig. 2.2, and the calorimeter and muon systems. It reduces the rate to 1 MHz at which the entire detector can be read out. This maximum rate is imposed by the front-end electronics [15]. The pile-up detector aims at distinguishing between crossings with single and multiple visible interactions, but in 2011 and 2012 it was only used for luminosity measurements [11]. Informations from the calorimeter and muon systems are used to trigger on the transverse energy (E_T) of hadron, electron and photon clusters in the calorimeters and on the transverse momentum (p_T) of one or two muon candidates in the muon chambers above a certain threshold. [14]

---

[1]An interaction is defined to be visible if it produces at least two charged particles with sufficient hits in the VELO and T1-T3 to allow them to be reconstructible. [14]

The HLT reduces the rate from 1 MHz to 5 kHz. It is divided into two stages, HLT1 and HLT2, and fully implemented in software, thus very flexible and subject to developments and adjustments following the evolution of the event reconstruction and selection software. The HLT runs on the Event Filter Farm (EFF), which is a farm of multiprocessor PCs.

A "trigger line" is composed of a sequence of reconstruction algorithms and selections. The trigger line returns an accept or reject decision. An event will be accepted by L0, HLT1 or HLT2 if it is accepted by at least one of its trigger lines at the relevant stage [15].

2.8 Stripping

After a full offline reconstruction of the data a so called stripping is applied, which is in principle applying commonly used pre-selection agorithms on the data [3, 18]. The idea behind this stripping is saving time for the individual analyses and providing consistent selections for basic particles or decays.

3 Data sample

The same data sample as in [3] was used. The data was collected from pp collisions at a centre of mass energy of 8 TeV in 2012 by the LHCb detector and corresponds to a total integrated luminosity of 2 fb^{-1} [3]. Collisions were recorded for both magnet polarities at similar fractions. The direction of the magnetic field is along the positive y axis for the MagUp and along the negative y axis for the MagDown polarity configuration [16]. For the analysis described in this thesis a simulated Monte Carlo (MC) sample with $Z \to \mu^+\mu^-$ events generated at the same centre of mass energy with both magnet polarities was used. The simulated pp collisions are generated using PYTHIA 6 [17] with a specific LHCb configuration. Decays of hadronic particles are described by EVTGEN in which final state radiation is generated using PHOTOS. The interaction of the generated particles with the detector, and its response, are implemented using the GEANT4 toolkit. For both simulated and measured data the same triggers as well as the same stripping and selection cuts were applied.

3.1 Trigger

An event candidate is triggered by requiring in a first step (L0), that at least one muon has a transverse momentum (p_T) higher than 1.5 GeV/c and that there are less than 600 hits in the scintillating pad detector (nSPDHits). This latter cut, called global event cut, is applied to reject high particle multiplicity events, which would dominate the processing time in the further reconstruction. In a second step (HLT1), one reconstructed muon must have a p_T of more than 4.8 GeV/c and a momentum (p) larger than 8 GeV/c. Furthermore, the χ^2 per degree of freedom (χ^2/ndf) of the track fit has to be smaller than four. In the last step (HLT2) of this trigger line, it is required that at least one muon has a p_T greater than 10 GeV/c [3]. All three steps combined are called high-p_T single muon trigger line and the required cuts are summarised in Table 3.1.

Trigger level	Condition
L0	$p > 1.5$ GeV/c
	nSPD hits < 600
HLT1	$p > 8$ GeV/c
	$p_{\mathrm{T}} > 4.8$ GeV/c
	track $\chi^2/\mathrm{ndf} < 4$
HLT2	$p_{\mathrm{T}} > 10$ GeV/c

Table 3.1: Trigger requirements for one muon of the high-p_{T} single muon trigger line.

3.2   Stripping

In this analysis the stripping line Z02MuMuLine is used. This line requires one muon with $p_{\mathrm{T}} > 3.0$ GeV/c from the StdAllLooseMuons particle container and a dimuon invariant mass of $M_{\mu^+\mu^-} > 40$ GeV/c^2.

3.3   Selection

Z candidates are built from two tracks of opposite charge, which are well reconstructed and identified as muons [3]. In addition, at least one of the two tracks has to satisfy the requirements of the high-p_{T} single muon trigger line. Each of the tracks, that are identified as muons, must have a $p_{\mathrm{T}} > 20$ GeV/c and lie in the pseudorapidity range of $2 < \eta < 4.5$, as motivated by the detector acceptance. Fig. 3.1 shows the distributions of p_{T} and η for both positively and negatively charged muons. Events are combined for the two magnet polarities.
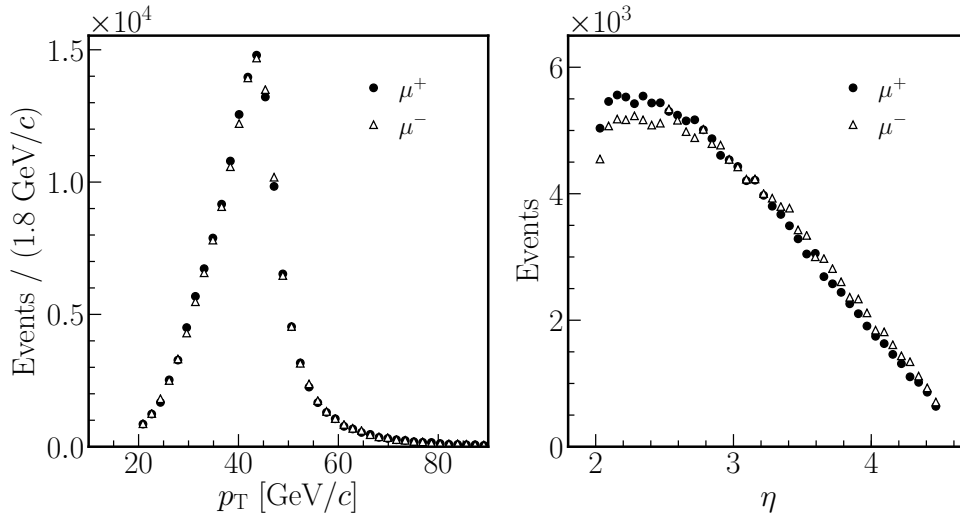

Figure 3.1: Distribution of the transverse momenta (left) and of the pseudorapidity (right). Filled circles (triangles) are positively (negatively) charged muons.

Two cuts are applied on the track quality: the probability χ^2 per degree of freedom of the track fit ($\mathrm{Prob}(\chi^2_{\mathrm{trk}}, \mathrm{ndf})$) must be larger than 0.1% and the relative uncertainty on the momentum measurement has to be less than 10%. Furthermore the combined dimuon

17

mass, $M_{\mu^+\mu^-}$ has to be in the range of $60 < M_{\mu^+\mu^-} < 120$ GeV/c^2. Fig. 3.2 shows the invariant mass distribution of the selected Z candidates in data and Table 3.2 summarises the selection cuts.
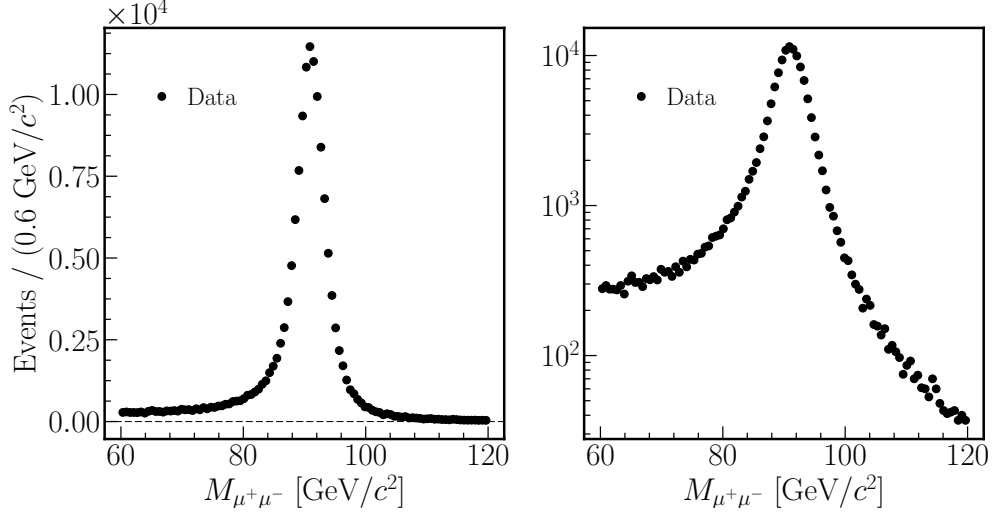

Figure 3.2: The invariant mass $M_{\mu^+\mu^-}$ is shown. Logarithmic representation on the right. The left tail comes from photon radiation of the muons and contributions from the Drell-Yan γ^* production and γ^*Z interference.

Variable	Condition
Muons	$p_{\mathrm{T}} > 20$ GeV/c
	$2 < \eta < 4.5$
	$\mathrm{Prob}(\chi^2_{\mathrm{trk}}, \mathrm{ndf}) > 0.001$
	$\sigma_p/p > 0.1$
Z candidate	$60 < M_{\mu^+\mu^-} < 120$ GeV/c^2
Trigger for one muon	high-p_{T} single muon trigger line

Table 3.2: Selection cuts for both muons.

From the studies in reference [18] it is known that the purity, defined as the ratio of signal to total candidate events, is almost 100%. Backgrounds from misidentified muons or from the decay of hadrons containing heavy quarks contribute less than 0.3%. Therefore, background contributions to the Z are neglected in the further analysis. The tail on the left of the Z peak consists of two contributions. One part is the radiative tail of Z events, due to photon radiation of the muons (final state radiation). Another part is coming from the Drell-Yan γ^* production and γ^*Z interference, which also contribute to the tail on the right, but on a smaller scale. In the following, Z always includes γ^* and γ^*Z. In total 144'293 Z $\rightarrow \mu^+\mu^-$ candidates are selected in data, 190'275 candidates in MC.

4   Analysis

4.1   Angles in the lab frame

To calculate the angles, the momenta of the particles from the provided data sample are used. The polar angle (θ) is given by Eq. (1) and the azimuthal angle (ϕ) by Eq. (2). For both angles only the values for the muons of positive charge were used for the further analysis. When reversing the resulting angles of the negative charged muons in the rest frame of the decaying Z boson by subtracting an angle of π, comparison shows almost perfect agreement, hence the omission is made without further remark.

Figure 4.1 shows the raw polar angle distribution of data and the MC simulation for the two magnet polarities (MagUp and MagDown) in the lab frame. MC events are normalized to the total number of events in data. The ratio data/MC is consistent with one to about $\theta \approx 240$ mrad for both magnet polarities, whereas for largest θ less events are generated in simulation than in data. There is no obvious detector effect that could be identified, but these deviations could occur due to higher order effects, that are not included in MC, or differences in the parton distribution function. The abrupt change in the distribution towards both ends of the theta range, for $\theta \lesssim 40$ mrad and $\theta \gtrsim 260$ mrad, comes from the limited angular coverage of the detector and its reduced acceptance in this region.
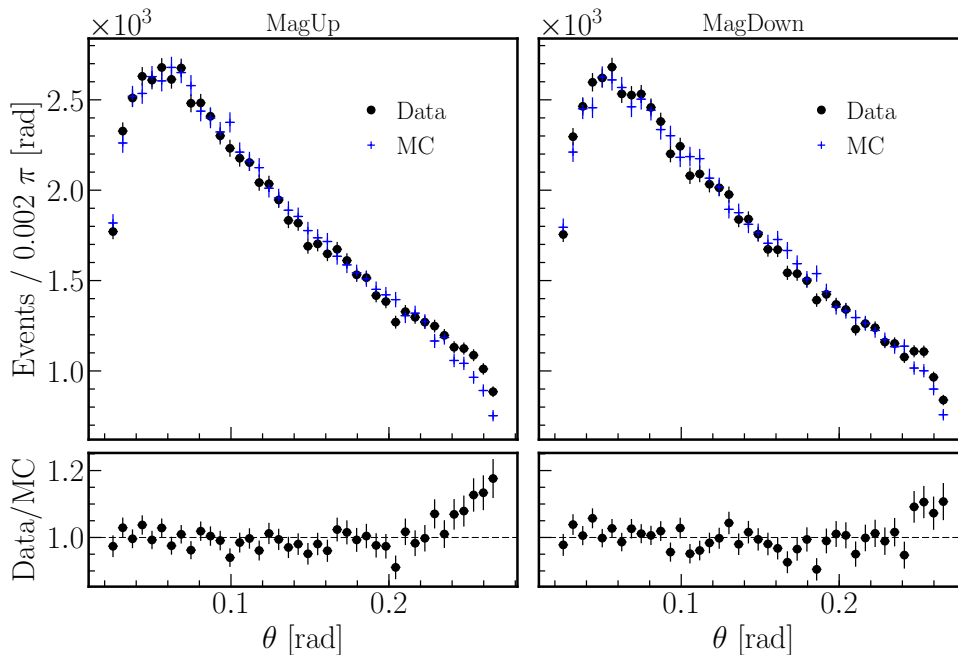

Figure 4.1: Distributions of the polar angle in the lab frame for MagUp (left) and MagDown (right). Data is shown with black circles, MC with blue plusses and is normalized to the number of data events. The lower panels show the data-to-MC ratios. Error bars represent statistical uncertainties only.

Figure 4.2 shows the azimuthal angle (ϕ) distribution of data and simulation for the two magnet polarities in the lab frame. Again, events generated from MC are normalized to the number of data events. Both data and simulation feature less events in the regions of

$\phi \approx \pm\pi/2$ and $\phi \approx 0$ rad, which is due to overlaps of modules in the VELO resulting in a higher detector thickness seen by particles passing through this region of the detector [14]. However, these effects only seem to be taken partly into account by MC. Since we are expecting a flat distribution in the lab frame without detector characteristics, weights were applied to the MC simulation to achieve a uniform distribution of the ratio Data/MC. These weights were applied in all uses of MC for the complete analysis.
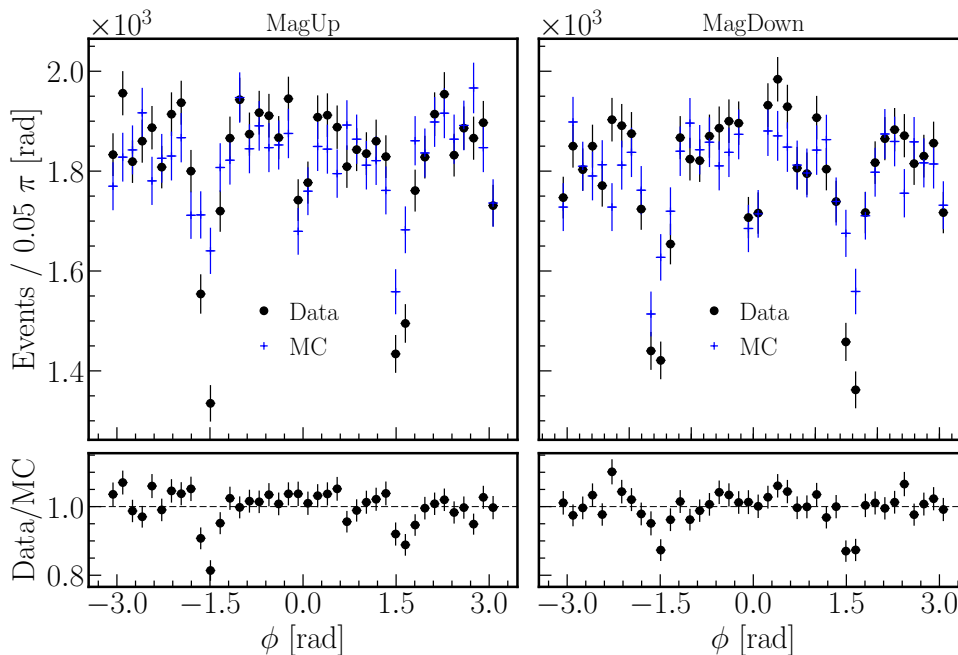

Figure 4.2: Distributions of the azimuthal angle in the lab frame for MagUp (left) and MagDown (right). Data is shown with black circles, MC with blue plusses and is normalized to the number of data events. The lower panels show the data-to-MC ratios. Error bars represent statistical uncertainties only.

4.2   Angles in the Collins-Soper frame

To get the momenta of the muons in the Collins-Soper (CS) frame, and thus calculating the angles in that reference frame, a transformation following the steps in Section 1.4 is necessary. Using the transformed momenta of the muons, the polar angle θ^* and the azimuthal angle ϕ^* in the CS frame are given by Eq. (3) and Eq. (4), respectively.

The distribution of the polar angle in the CS frame ($\cos\theta^*$) is shown in Fig. 4.3. Statistically sufficient numerous events are in the angular region of $-0.75 \lesssim \cos\theta^* \lesssim 0.75$. Only few events outside this range are available, which is dealt with in Section 4.4. The distribution of the azimuthal angle (ϕ^*) in the CS frame (Fig. 4.4) shows a noticeable change compared to the one in the lab frame (Fig. 4.2), which is also discussed in Section 4.3. Both data and MC behave similarly and their ratio has only small deviations from 1.
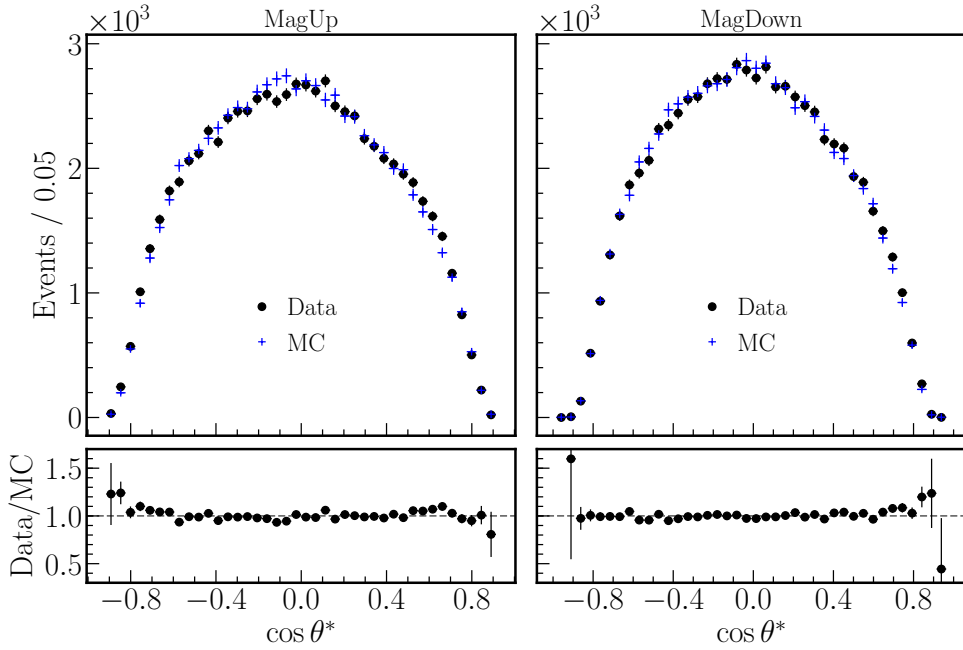
Figure 4.3: Distributions of the cosine of the polar angle in the CS frame for MagUp (left) and MagDown (right). Data is shown with black circles, MC with blue plusses and is normalized to the number of data events. The lower panels show the data-to-MC ratios. Error bars represent statistical uncertainties only.
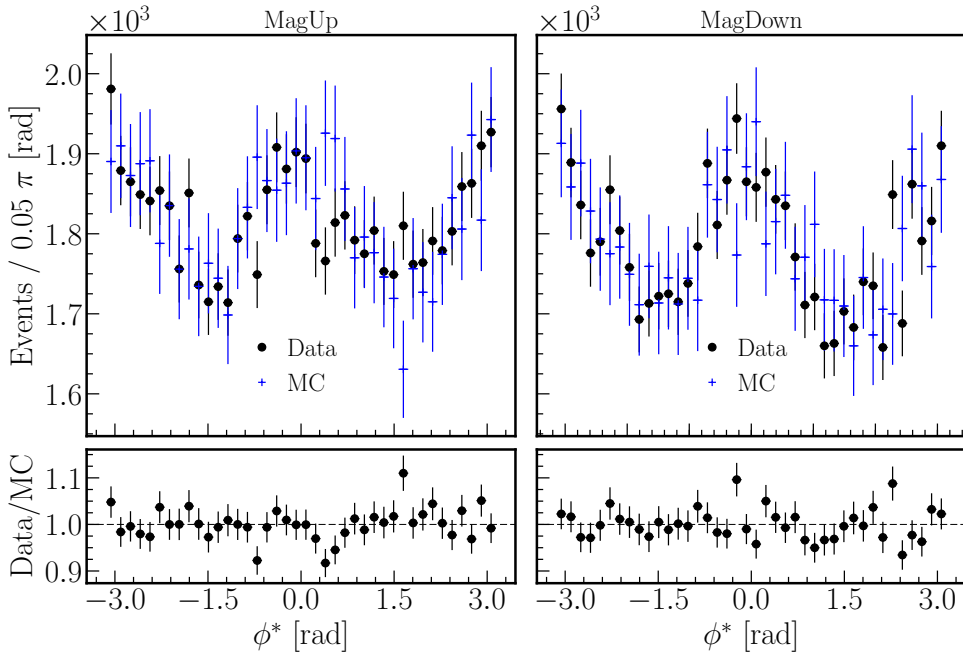

Figure 4.4: Distributions of the azimuthal angle in the CS frame for MagUp (left) and MagDown (right). Data is shown with black circles, MC with blue plusses and is normalized to the number of data events. The lower panels show the data-to-MC ratios. Error bars represent statistical uncertainties only.

4.3 Reweighting

The comparison between data and simulated events shows a significant difference in the distribution of multiplicity variables. Figure 4.5 shows the distributions for the number of tracks (nTracks), the number of long tracks (nLongTracks) and the number of hits in the Scintillating Pad Detector (nSPDHits). If this led to a different behaviour for the angular distributions of data and MC, a correction in the form of a reweighting would be necessary. This could be the case because the tracking efficiency is lower for a larger number of tracks per event and the primary vertex resolution is strongly correlated to the number of tracks in the vertex, as discussed in Sections 2.3 and 2.4.

Different approaches for a reweighting have been studied, but all were discarded because they had no effect on the acceptance of both $\cos\theta^*$ and ϕ^*. The multiplicity variables plotted as a function of $\cos\theta^*$ and ϕ^*, shown in Fig. 4.6 for MagUp[2], are not all completely independent of the angle and thus do not agree well enough with a straight line fit with a slope of zero. However, the ratios of data and MC are rather flat and do agree well with a fit to a straight line in most cases. This means that angular dependencies of the multiplicity variables, that predominantly come from detector effects, are implemented well enough in MC.

To quantify this, the slope parameters with statistical uncertainty only and the goodness of the fit are summarised in Table 4.1. All slopes are consistent with a value of zero at one standard deviation (σ) except for the slopes of nTracks and nLongTracks as a function of ϕ^* of MagDown, which are 1.2σ and 1.3σ off, respectively. The goodness of the fits is reasonable for all combinations, even though for the number of long tracks as a function of $\cos\theta^*$ for MagUp the values stand out, which is mainly due to a single outlier in the center. Since all other values and the other magnet polarisation show no deviations, it was concluded that no reweighting is necessary.

4.4 Acceptance correction

To get the true angular distribution of the Z bosons decaying to two muons, the data has to be corrected by the acceptance. The acceptance corrects for the geometry of the detector and its efficiencies, such as the reconstruction, trigger and selection efficiency. Absolute values are not relevant for this analysis and thus have not been calculated. However, due to the limited pseudorapidity range of the detector, a strong dependence of the acceptance on the polar angle is expected, and we have to correct for this. An estimate of the acceptance is made using MC simulation. This is done separately for the two magnet polarities by computing the number of events within a certain angular range i divided by the number of events that is expected in a certain bin in the CS frame:

$$\text{acc}[i] = \frac{\#\text{ events generated by MC in bin i}}{\#\text{ events expected from physics of MC in bin i}} \tag{11}$$

However, it was difficult to make an estimate for MC without detector effects for LHCb, because there did not exist a sample of that kind at the time. For that reason, for the calculation of the acceptance, the assumption was made, that MC behaves like leading

---

[2]The distributions for the negative magnet polarity (MagDown) are shown in Fig. A.2.

		ϕ^*		
Polarity	Variable	Slope	χ^2/ndf	p-value
MagUp	nTracks	-0.0014 ± 0.0019	1.02	0.43
	nLongTracks	-0.0020 ± 0.0019	1.02	0.43
	nSPDHits	-0.0016 ± 0.0020	0.89	0.58
MagDown	nTracks	-0.0018 ± 0.0015	0.99	0.47
	nLongTracks	-0.0018 ± 0.0014	0.56	0.93
	nSPDHits	-0.0005 ± 0.0018	0.68	0.83
		$\cos\theta^*$		
Polarity	Variable	Slope	χ^2/ndf	p-value
MagUp	nTracks	0.000 ± 0.009	1.21	0.24
	nLongTracks	-0.006 ± 0.010	1.48	0.09
	nSPDHits	0.000 ± 0.009	1.00	0.45
MagDown	nTracks	-0.001 ± 0.007	0.81	0.69
	nLongTracks	-0.000 ± 0.007	0.84	0.66
	nSPDHits	0.002 ± 0.008	0.75	0.76

Table 4.1: The value of the determined slope and its statistical uncertainty, the χ^2 per degree of freedom and the p-value of the fit of Figs. 4.6 and A.2 for ϕ^* (top) and $\cos\theta^*$ (bottom).

order physics. In that case all coefficients of Eq. (8) vanish except for A_4. With $A_4 = 0.052$ a mean value was used from measurements from [6].

Figure 4.7 shows the strong dependence of the acceptance on the polar angle. Without the limitations of the detector we would expect in MC a distribution of the form $1 + \cos^2\theta^* + A_4\cos\theta^*$ for the polar angle. Uncertainties are only statistical and are smaller or comparable with the marker size. Towards the two borders of the $\cos\theta^*$-range only very little statistics is available. This becomes especially evident and problematic when further dividing these ranges in the spectrum of the azimuthal angle ϕ^* for the 2D fit in Section 4.5. Hence for the regions at the border, bins had to be combined and an unequal binning was applied for the acceptance correction.

Figure 4.8 shows the acceptance as a function of ϕ^*. In this case, MC without detector effects is a constant. There seems to be an oscillation with maxima at $\phi^* = 0$ and $\phi^* = \pm\pi$ and minima at $\phi^* = \pm\pi/2$. These are potentially no detector effects, even though it's explicable that the acceptance is smaller in the region of $\phi^* = \pm\pi/2$ due to partly overlapping sensors in the VELO. However, it is expected to be smaller for $\phi^* = 0$ as well an this is not the case. Additionally the oscillation looks quite smooth, which isn't the case in Fig. 4.2, where the detector effects are visible. So it's possible that the underlying physics of MC also has a ϕ^* dependence, which we do not account for. Because the physics of MC is simply constant for ϕ^*, MC and the acceptance have exactly the same shape.

To account for both angular dependencies of the acceptance, a sequential 1D calculation of the acceptance of each angle was done. A 2D calculation was taken into consideration, but was discarded because that meant choosing between either lower statistics per bin and thus larger statistical relative uncertainties or coarser binning and hence less precision. The acceptance was first calculated for ϕ^* and then for $\cos\theta^*$. To avoid including the same effects twice, the acceptance correction of ϕ^* was applied to MC before calculating the acceptance of $\cos\theta^*$.
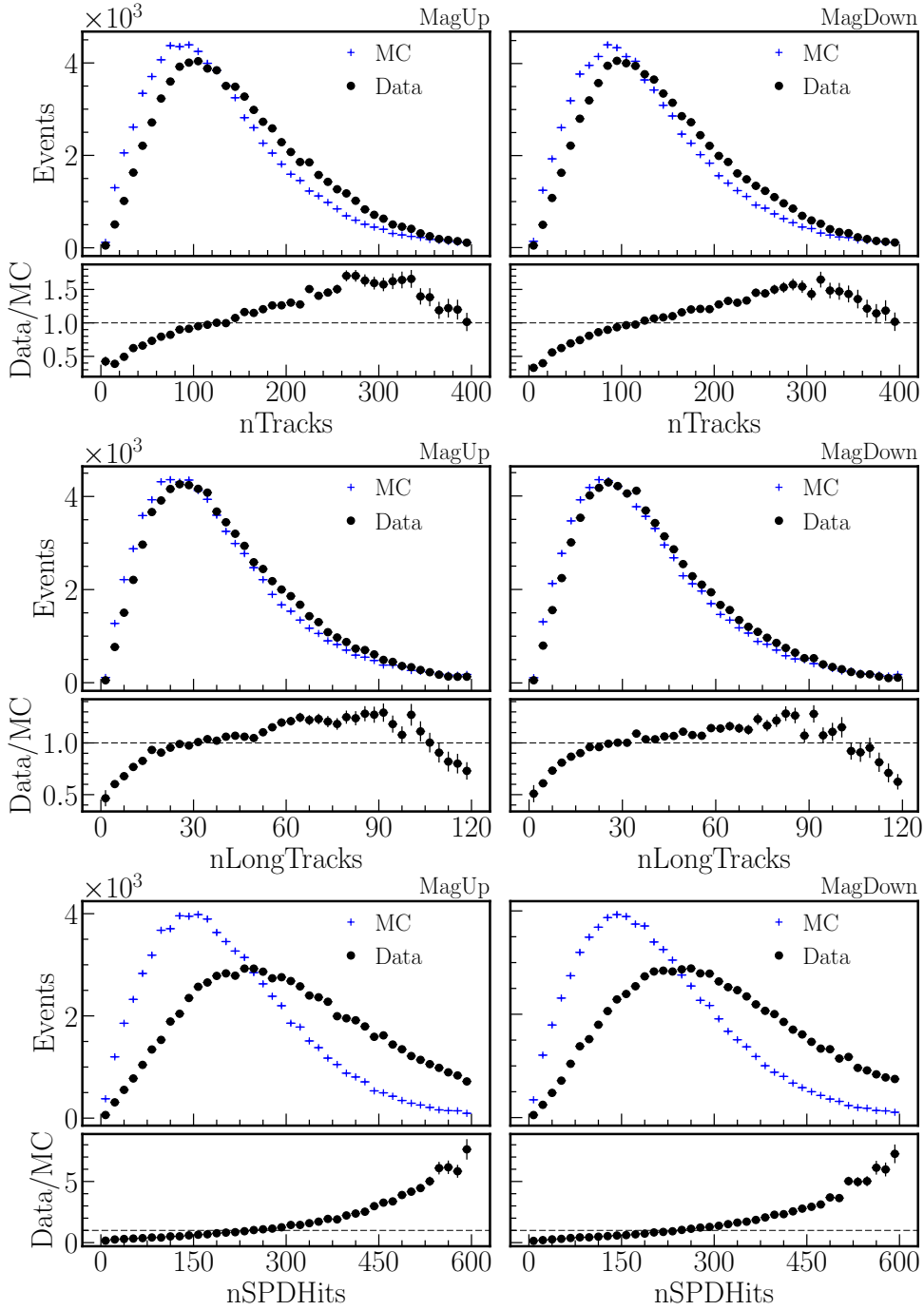
Figure 4.5: Distributions of the multiplicity variables. The number of tracks (top), the number of long tracks (middle) and the number of hits in the scintillating pad detector (bottom) for MagUp (left) and MagDown (right). Data is shown with black circles, MC with blue plusses and is normalized to the number of data events. The lower panels show the data-to-MC ratios. Error bars represent statistical uncertainties only.
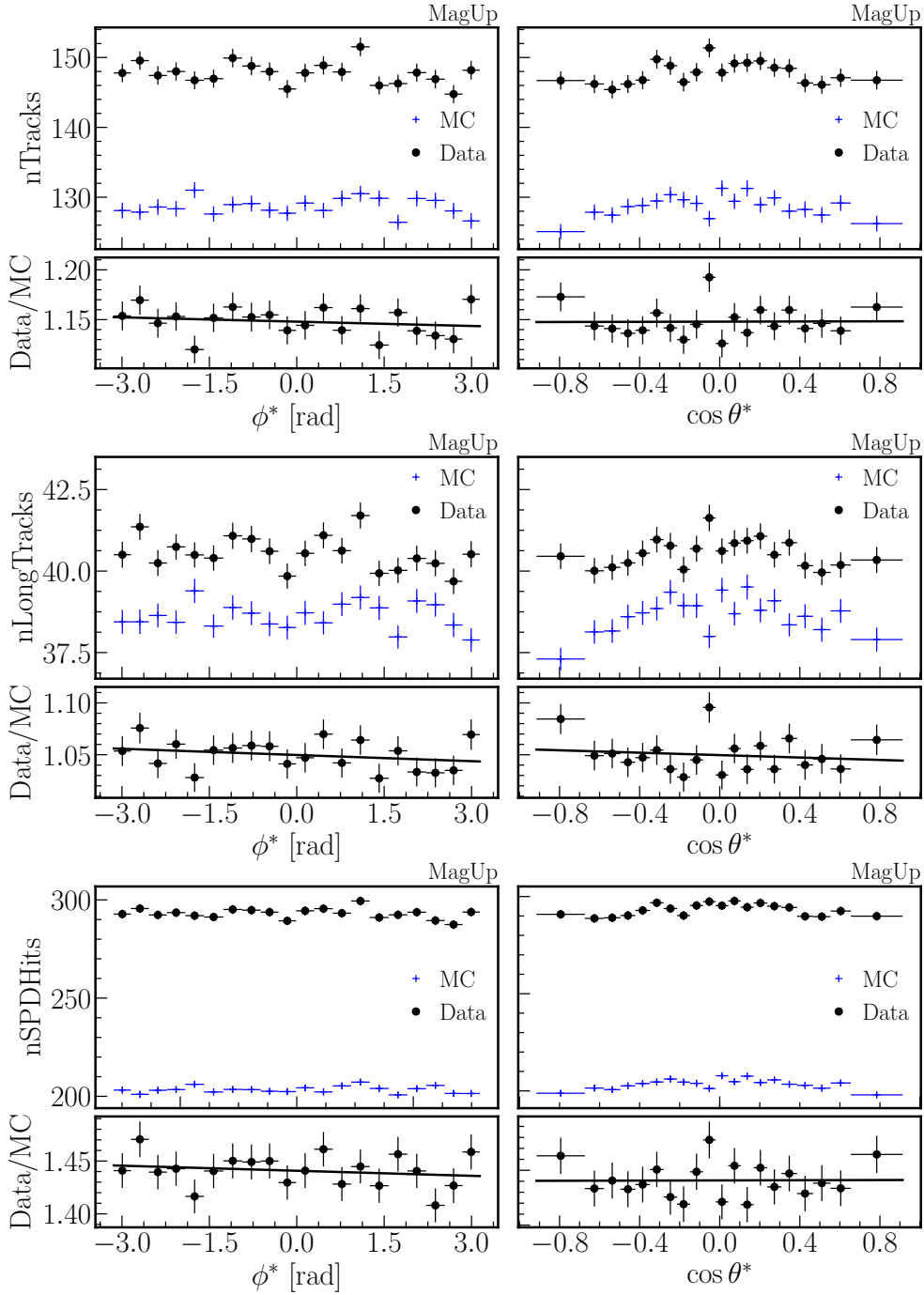
Figure 4.6: The number of tracks (top), the number of long tracks (middle) and the number of hits in the scintillating pad detector (bottom) as a function of ϕ^* (left) and $\cos\theta^*$ (right) for positive magnet polarity only. Data is shown with black circles, MC with blue plusses. The lower panels show the data-to-MC ratios with the straight line fit. Error bars represent statistical uncertainties only.
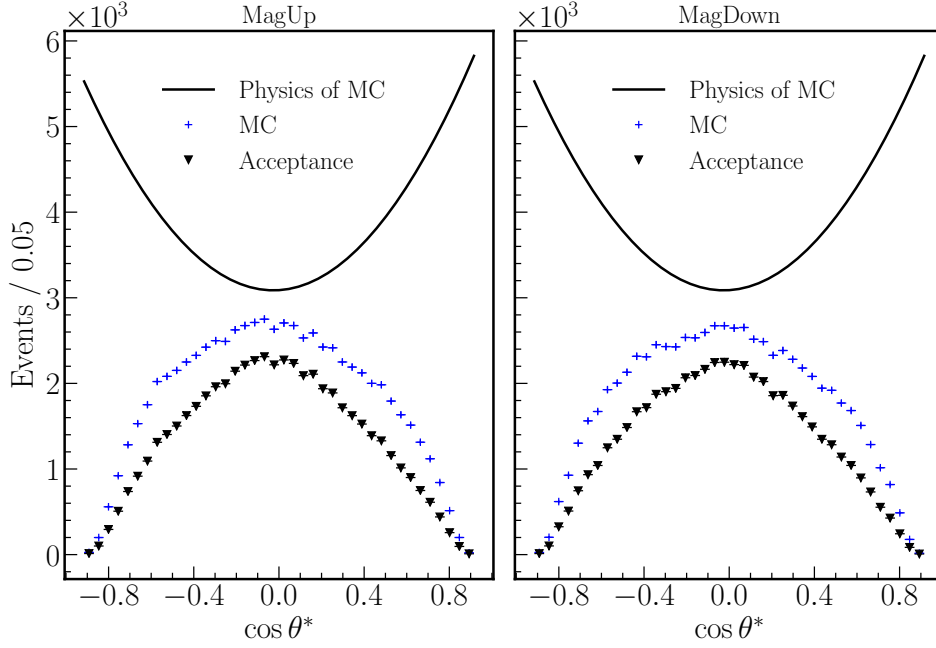
Figure 4.7: Acceptance of $\cos\theta^*$ for MagUp (left) and MagDown (right) shown with black triangles, MC with blue plusses. The black line shows the distribution that is implemented in MC without detector effects and is of the form $1 + \cos^2\theta^* + A_4\cos\theta^*$. The scale of the y-axis applies to MC events. The physics of MC and the acceptance are normalized to a value, that ensures good readability. Vertical bars represent statistical uncertainties only.
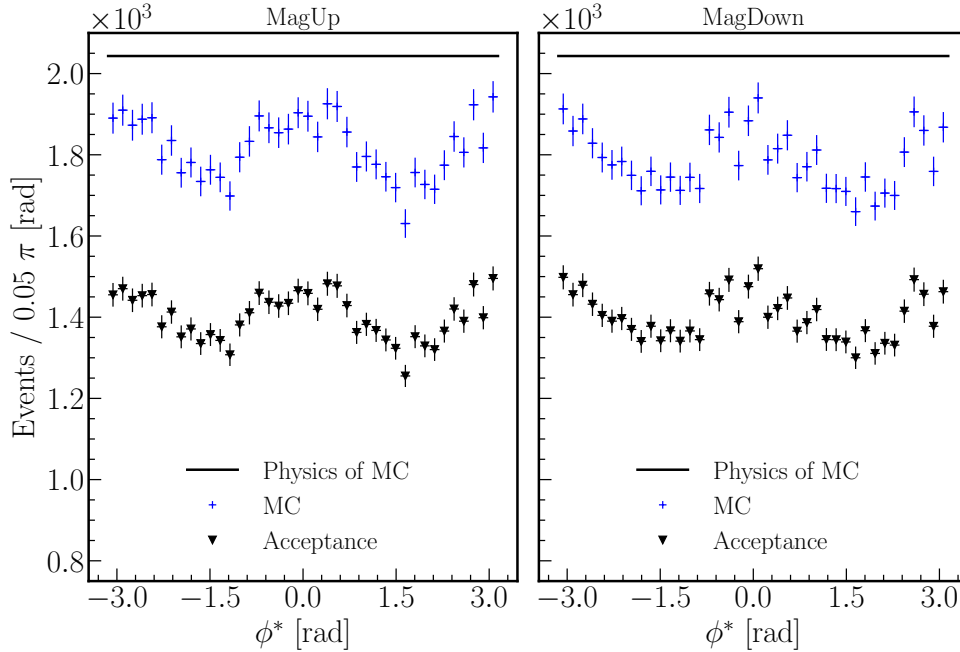

Figure 4.8: Acceptance of ϕ^* for MagUp (left) and MagDown (right) shown with black triangles, MC with blue plusses. The black line shows the distribution that is implemented in MC without detector effects and is of the form of a constant function. The scale of the y-axis applies to MC events. The physics of MC and the acceptance are normalized to a value, that ensures good readability. Vertical bars represent statistical uncertainties only.

4.5   Fit to PDF

The complete acceptance corrected data as a function of the two angles ϕ^* and $\cos\theta^*$ in the CS frame is illustrated in Fig. 4.9 for both magnet polarities combined. For the 2D plot a coarser binning was chosen to ensure sufficient statistics per single bin. Even though the binning might seem very conservative, it has to be considered that towards the ends of the $\cos\theta^*$ scale only few events are available, however, the weights from the acceptance are extremely large. The projection plots use the same binning that has been used throughout this analysis. In the projection plot of $\cos\theta^*$ the same unequal binning that was used for the calculation of the acceptance correction is depicted.
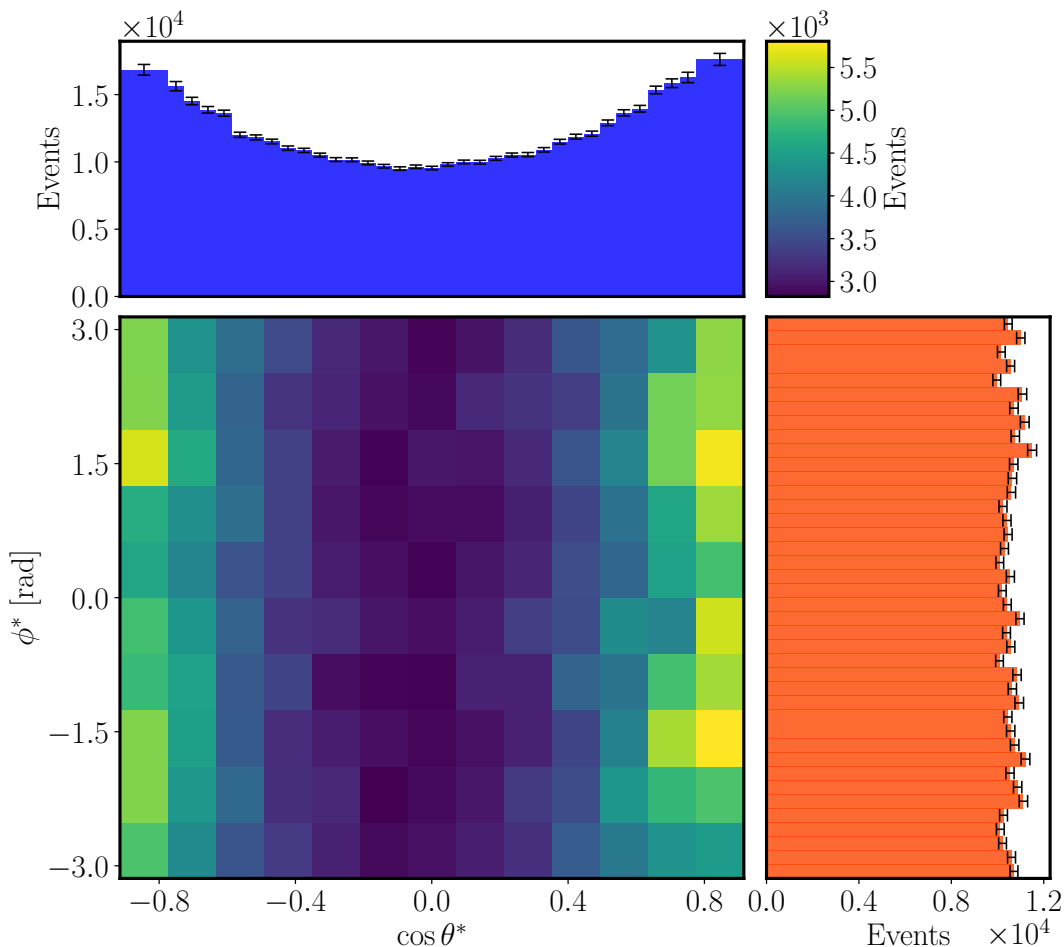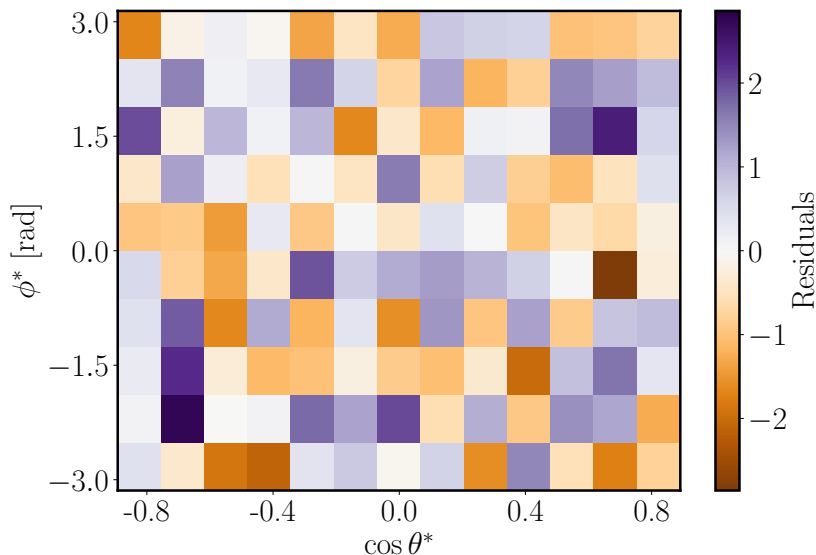

Figure 4.9: 2D angular distribution of data in the CS frame. Projection of $\cos\theta^*$ (top) with larger bin at the border and projection of ϕ^* (right). The complete data from both magnet polarities is combined. Error bars in projection plots represent statistical uncertainties only.

For the 2D fit of Eq. (8), the data has been divided into different ranges of the transverse momentum of the Z boson (p_T^Z). Four regions with the following boundaries were defined: $p_T^{Z,\text{boundary}}$ [GeV/c] = $\{0,\ 10,\ 20,\ 30,\ \infty\}$. For each region the acceptance was calculated individually and events from the two opposite magnet polarities were combined at the end. For the different p_T^Z-ranges the following values of A_4 were used for the acceptance correction, taken from measurements from [6].

$p_{\mathrm{T}}^{\mathrm{Z}}$ [GeV/c]	$0 - 10$	$10 - 20$	$20 - 30$	> 30
A_4	0.065 ± 0.002	0.061 ± 0.003	0.057 ± 0.003	0.033 ± 0.008

Table 4.2: Values for A_4 with statistical uncertainties taken from measurements from [6].

The data was fitted using a binned least square method with Poisson uncertainties. The fits converge and the 2D residual plots show no systematic patterns. Fig. 4.10 illustrates the 2D residuals for $10 < p_{\mathrm{T}}^{\mathrm{Z}} < 20$ GeV/c. 61.5% of the uncertainties are within 1σ. Only statistical uncertainties have been used for the calculation of the residuals. The plots of the other $p_{\mathrm{T}}^{\mathrm{Z}}$-ranges can be found in Appendix A.3. Their percentages within 1σ are 71.5%, 64.6% and 64.6% for the ranges in increasing order of $p_{\mathrm{T}}^{\mathrm{Z}}$.

Figure 4.10: Residuals of 2D angular distribution for $10 < p_{\mathrm{T}}^{\mathrm{Z}} < 20$ GeV/c. Data from both magnet polarities is combined. 61.5% of the uncertainties are within 1σ. Residuals are calculated only from statistical uncertainties.

The number of events and the goodness of the fit in the form of the chi-squared per degree of freedom (χ^2/ndf) and the p-value are listed in Table 4.3.

$p_{\mathrm{T}}^{\mathrm{Z}}$ [GeV/c]	$0 - 10$	$10 - 20$	$20 - 30$	> 30
Events	72962	37291	15814	18183
χ^2/ndf	1.19	1.30	1.41	1.38
p-value	0.07	0.02	0.002	0.004

Table 4.3: Number of events and goodness of the 2D fit for the four $p_{\mathrm{T}}^{\mathrm{Z}}$-ranges.

Three of the four fits in the respective ranges have a p-value < 0.05, which tells us that the quality of the fit is not good enough to draw any conclusions from their results. Only

for $0 < p_T^Z < 10$ GeV/c the p-value is above 0.05, for $10 < p_T^Z < 20$ GeV/c it is 0.02 and for higher p_T^Z it is less than 0.01. The extracted angular coefficients $A_{i=0,\ldots,7}$ are listed in Table 4.5 and visualised in Fig. 4.13.

A crude estimate of a systematic uncertainty was obtained by calculating the acceptance of $\cos\theta^*$ (Section 4.4) with an alternate function. Instead with the $1 + \cos^2\theta^* + A_4\cos\theta^*$ distribution of MC, the calculation of the acceptance was done with a correction to a $1 + \cos^4\theta^*$ distribution. With this alternate acceptance the calculation of the angular coefficients was repeated. From the resulting difference between the coefficients, calculated in the two different ways, the systematic uncertainty on the angular coefficients $A_{i=0,\ldots,7}$ was estimated. It is clear that for better results, a more sophisticated toy model would need to be considered. Due to the dependence only on θ^*, the systematic uncertainties are varying strongly between the different coefficients, because they depend unequally on the polar angle.

Fig. 4.11 shows the projections of the two angles in the same p_T^Z-range as the figure above. The projection of the fit shows that ϕ^* is not constant. However only 40.0% of the uncertainties are within 1σ. For the distribution of $\cos\theta^*$ a clear asymmetry is visible. 62.9% of the uncertainties are within 1σ. The projection plots of the other ranges can be found in Appendix A.4.
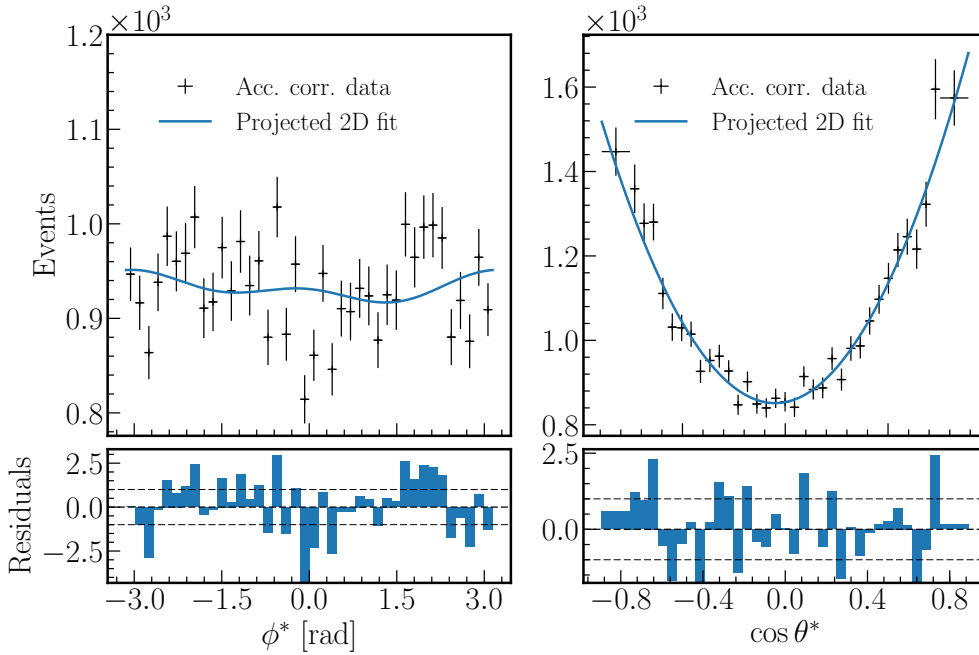

Figure 4.11: Projections of 2D fit (blue line) to acceptance corrected data (black plusses) for ϕ^* (left) and $\cos\theta^*$ (right) for $10 < p_T^Z < 20$ GeV/c. Error bars show statistical uncertainties only. The lower panels show the residuals. 40.0% (ϕ^*) and 62.9% ($\cos\theta^*$) of the uncertainties are within 1σ.

Because the projected functions of the 2D fit do visually not agree well with the acceptance corrected data, especially in the case of ϕ^*, a 1D fit of the angular distribution was done, to analyse whether a better fit can be achieved. This might be the case, because all coefficients, except A_0 and A_4 depend on both angles. As a consequence, the information about A_1 and A_6 is lost. For the fit of ϕ^* Eq. (9) is used and for $\cos\theta^*$ Eq. (10). For the calculation of the acceptance only the contribution of the respective angle is used, so the

acceptance corrected data will not necessarily be identical. Fig. 4.12 shows the 1D fit for $10 < p_T^Z < 20$ GeV/c, the plots for the other ranges can be found in Appendix A.5.
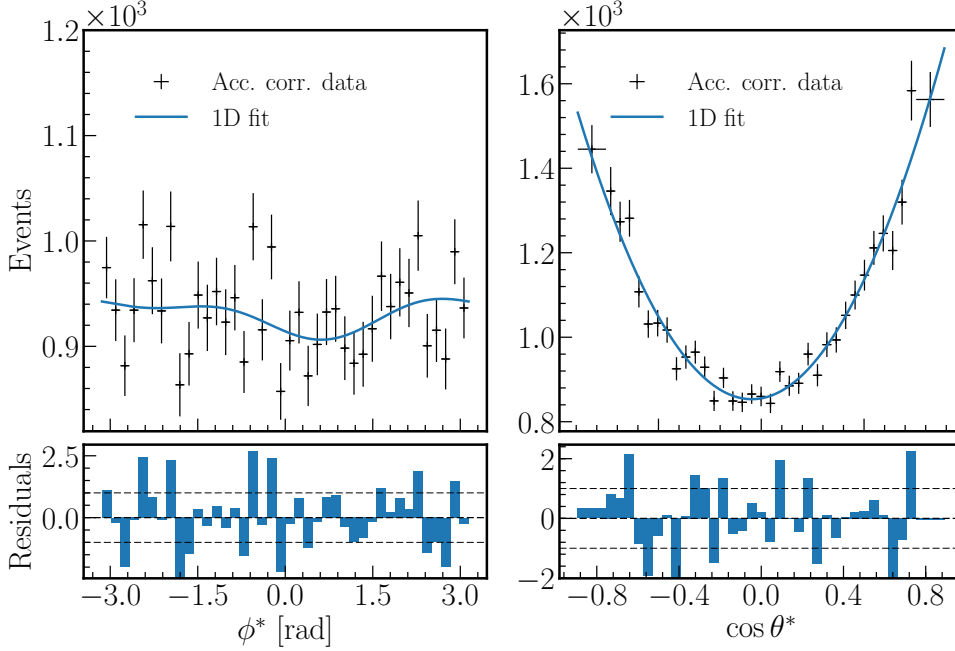

Figure 4.12: 1D fit (blue line) to acceptance corrected data (black plusses) for ϕ^* (left) and $\cos\theta^*$ (right) for $10 < p_T^Z < 20$ GeV/c. Error bars show statistical uncertainties only. The lower panels show the residuals. 60.0% (ϕ^*) and 65.7% ($\cos\theta^*$) of the uncertainties are within 1σ.

The 1D fits look like an improvement to the projected 2D fits. However, the goodness of the fits (Table 4.4) is numerically worse than the values of the 2D fits in five of eight cases.

	ϕ^*			
p_T^Z [GeV/c]	$0-10$	$10-20$	$20-30$	>30
χ^2/ndf	1.25	1.92	2.11	2.29
p-value	0.15	<0.01	<0.01	<0.01
	$\cos\theta^*$			
p_T^Z [GeV/c]	$0-10$	$10-20$	$20-30$	>30
χ^2/ndf	1.68	1.31	1.97	1.09
p-value	0.01	0.11	<0.01	0.33

Table 4.4: Goodness of the 1D fits for ϕ^* (top) and $\cos\theta^*$ (bottom) for the four p_T^Z-ranges.

Especially in ϕ^* seems to be a problem, with three p-values of less than 0.01. Only in the lowest p_T^Z-range the quality of the fit is good. The fits of the $\cos\theta^*$ distribution works reasonably well for $10 < p_T^Z < 20$ GeV/c and even better for $p_T^Z > 30$ GeV/c, however the other two ranges are in the order of 0.01 or less. The extracted angular coefficients A_0,

A_{2-5} and A_7 from the 1D fit, are depicted in Fig. 4.13. A study of systematic uncertainties has been omitted for the 1D fits.

4.6 Results

Being aware that the quality of the fits is somewhat questionable, the angular coefficients are extracted from the 2D and 1D fits and visualised in Fig. 4.13 and the coefficients from the 2D fits are listed in Table 4.5. In Fig. 4.13 a comparison is made, where values are available, with theoretical predictions from [4] at NNLO and measurements from the ATLAS ([6]) and CMS ([10]) collaboration. Theoretical predictions specifically for LHCb are only available for A_0, A_1 and A_2. Comparison with ATLAS and CMS has to be handled with care, because their analyses examined the coefficients in rapidity ranges outside the acceptance of LHCb.

p_T^Z [GeV/c]	A_0	A_2	$A_0 - A_2$
$0 - 10$	$0.008 \pm 0.018 \pm 0.280$	$-0.007 \pm 0.015 \pm 0.001$	$0.015 \pm 0.023 \pm 0.281$
$10 - 20$	$-0.048 \pm 0.025 \pm 0.270$	$0.032 \pm 0.021 \pm 0.001$	$-0.080 \pm 0.033 \pm 0.271$
$20 - 30$	$-0.10 \pm 0.04 \pm 0.27$	$0.100 \pm 0.033 \pm 0.004$	$-0.11 \pm 0.05 \pm 0.27$
> 30	$-0.250 \pm 0.034 \pm 0.240$	$-0.073 \pm 0.030 \pm 0.04$	$-0.177 \pm 0.05 \pm 0.28$
p_T^Z [GeV/c]	A_1	A_3	A_4
$0 - 10$	$0.000 \pm 0.011 \pm 0.001$	$-0.006 \pm 0.007 \pm 0.001$	$0.130 \pm 0.013 \pm 0.062$
$10 - 20$	$0.002 \pm 0.015 \pm 0.001$	$-0.016 \pm 0.010 \pm 0.002$	$0.110 \pm 0.019 \pm 0.058$
$20 - 30$	$0.011 \pm 0.025 \pm 0.001$	$0.008 \pm 0.016 \pm 0.001$	$0.077 \pm 0.031 \pm 0.058$
> 30	$0.003 \pm 0.023 \pm 0.001$	$0.004 \pm 0.014 \pm 0.001$	$-0.090 \pm 0.027 \pm 0.032$
p_T^Z [GeV/c]	A_5	A_6	A_7
$0 - 10$	$-0.001 \pm 0.007 \pm 0.001$	$-0.027 \pm 0.011 \pm 0.002$	$-0.003 \pm 0.007 \pm 0.001$
$10 - 20$	$-0.001 \pm 0.011 \pm 0.001$	$-0.019 \pm 0.016 \pm 0.001$	$-0.008 \pm 0.010 \pm 0.001$
$20 - 30$	$-0.013 \pm 0.016 \pm 0.001$	$-0.021 \pm 0.026 \pm 0.001$	$0.008 \pm 0.016 \pm 0.001$
> 30	$-0.027 \pm 0.014 \pm 0.004$	$0.025 \pm 0.023 \pm 0.001$	$0.017 \pm 0.014 \pm 0.002$

Table 4.5: Extracted angular coefficients $A_{i=0,\dots,7}$ with statistical and systematical uncertainty for the four p_T^Z-ranges from the 2D fit.

Looking at the extracted values of the angular coefficients $A_{i=0,\dots,7}$ in Fig. 4.13, we can see that the extracted values from the 2D and 1D fits agree with each other within their uncertainties. Compared to the other data points, there are large deviations. It seems like the negative value of A_0 would agree quite well to the references, which is odd, because looking at Eq. (8), we see that A_0 is a coefficient to the square of an uneven function. So this seems to be rather a coincidence than an ambiguity in the definition of the reference frame. A_1, A_3 and A_{5-7} are all relatively small, even at high p_T^Z less than 0.08, and are not expected to be determined precisely. However, almost all measurements at least agree with a value of zero. A_2, which like A_0 and A_1 is related to the polarization of the Z boson [10], does agree to the other data points for $p_T^Z < 30$ GeV/c. A_2 increases as a function of

p_T^Z, but the extracted value is negative for $p_T^Z > 30$ [GeV/c]. A_4, which is like A_3 sensitive to the V-A structure of the coupling of the muons [10], is close to agreement for the first three p_T^Z-ranges. Again for $p_T^Z > 30$ GeV/c a negative value is extracted, which can not be explained.

The extracted coefficients give a basic idea about their behaviour, but it is not a precise measurement. This leads back to the bad quality of the fit, which in turn can have several reasons. The most problematic step in the analysis was the acceptance correction. It was approximated that the underlying physics of MC without detector effects has an angular distribution of $1 + \cos^2\theta^* + A_4 \cos\theta^*$ in the CS frame. This incorporates physics only up to LO, neglecting higher-order terms. So it is most likely that we have used an incomplete model for the underlying physics in MC.

For the specific cases of A_1, A_3 and A_4, which are the only coefficients that show a significant η^Z dependence [6], dividing into different bins of η^Z might be one possibility to improve the measurements. Another possible step would be to further tighten the invariant mass window from $60 < M_{\mu^+\mu^-} < 120$ GeV/c^2 to $80 < M_{\mu^+\mu^-} < 100$ GeV/c^2 to minimise the contributions from γ^* and its interference with the Z boson. Furthermore the LHCb detector with its pseudorapidity acceptance of $2 \lesssim \eta \lesssim 5$ might not provide ideal conditions for a measurement of an angular distribution in θ.

Comparing the integrated luminosity of the three analyses, it has to be noted, that the CMS and ATLAS collaborations used data corresponding to 19.7 fb^{-1} and 20.3 fb^{-1} of pp collisions, respectively, while this analysis is based on 2 fb^{-1}.

5   Conclusion

A measurement of the eight angular coefficients $A_{i=0,...,7}$ for the production of Z bosons decaying to muon pairs as a function of p_T^Z is presented. The data corresponds to 2 fb^{-1} of pp collisions at a center of mass energy of $\sqrt{s} = 8$ TeV collected by the LHCb detector at the CERN LHC.

It has to be concluded, that this thesis cannot provide a precise measurement of these coefficients over multiple p_T^Z-ranges. Several reasons come into consideration and are discussed in more detail in Section 4.6. It is crucial to have a model, that describes the underlying physics of the simulated events to a high precision without detector effects. At the time of this analysis no accurate model of this kind existed for LHCb, but to achieve better results, this would be absolutely essential. To make further improvements, it has to be considered to divide the data into different ranges of η^Z. On a final note, the geometry of the LHCb detector with its reduced acceptance of η is perhaps not predestined for an angular analysis of this kind or requires more data to achieve similar results.
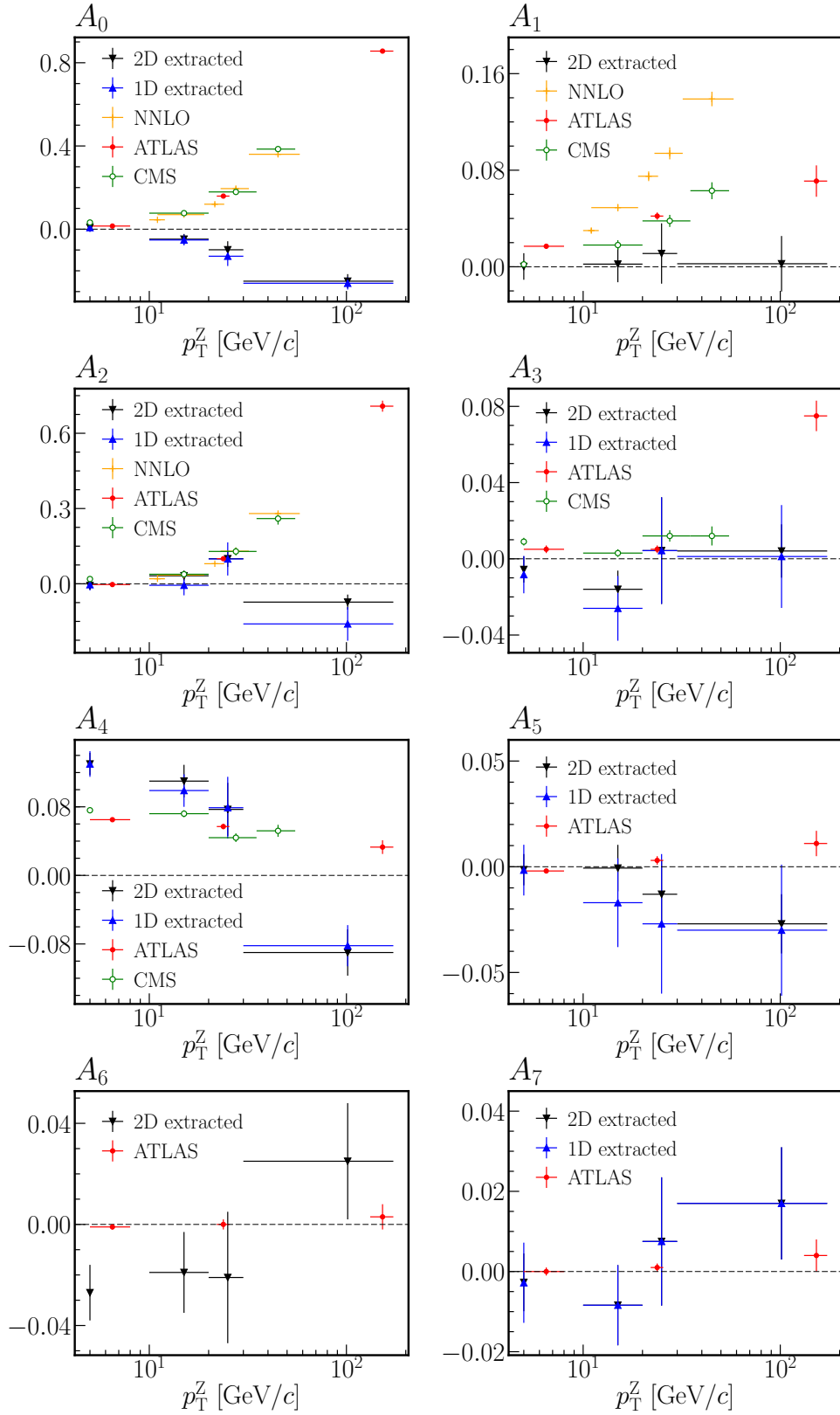
Figure 4.13: Angular coefficients $A_{i=0,...,7}$ as a function of $p_{\mathrm{T}}^{\mathrm{Z}}$. Results from the 2D fit (2D extracted) and 1D fit (1D extracted) are compared to theoretical predictions from [4] (NNLO) and measurements from [6] (ATLAS) and [10] (CMS), where values are available. Error bars represent statistical uncertainties only.
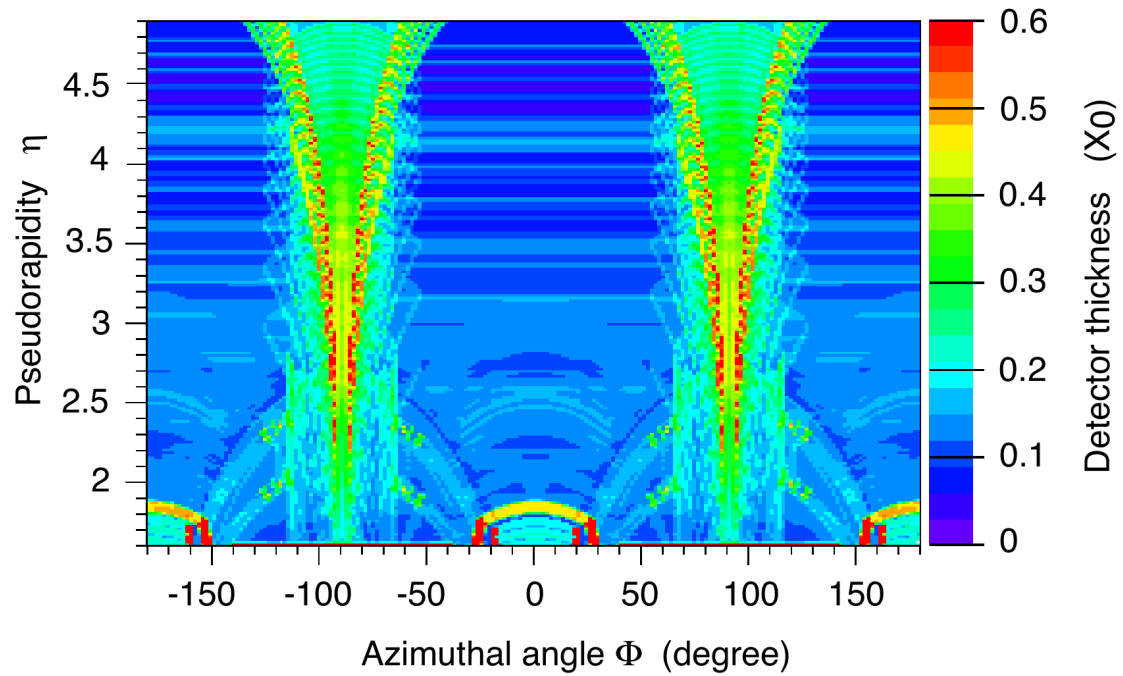
A   Appendix A

A.1   Detector thickness

Figure A.1: The average detector thickness seen by particles passing through the VELO as a function of azimuthal angle, ϕ, and pseudorapidity, η [14].

A.2   Angular distribution for MagDown
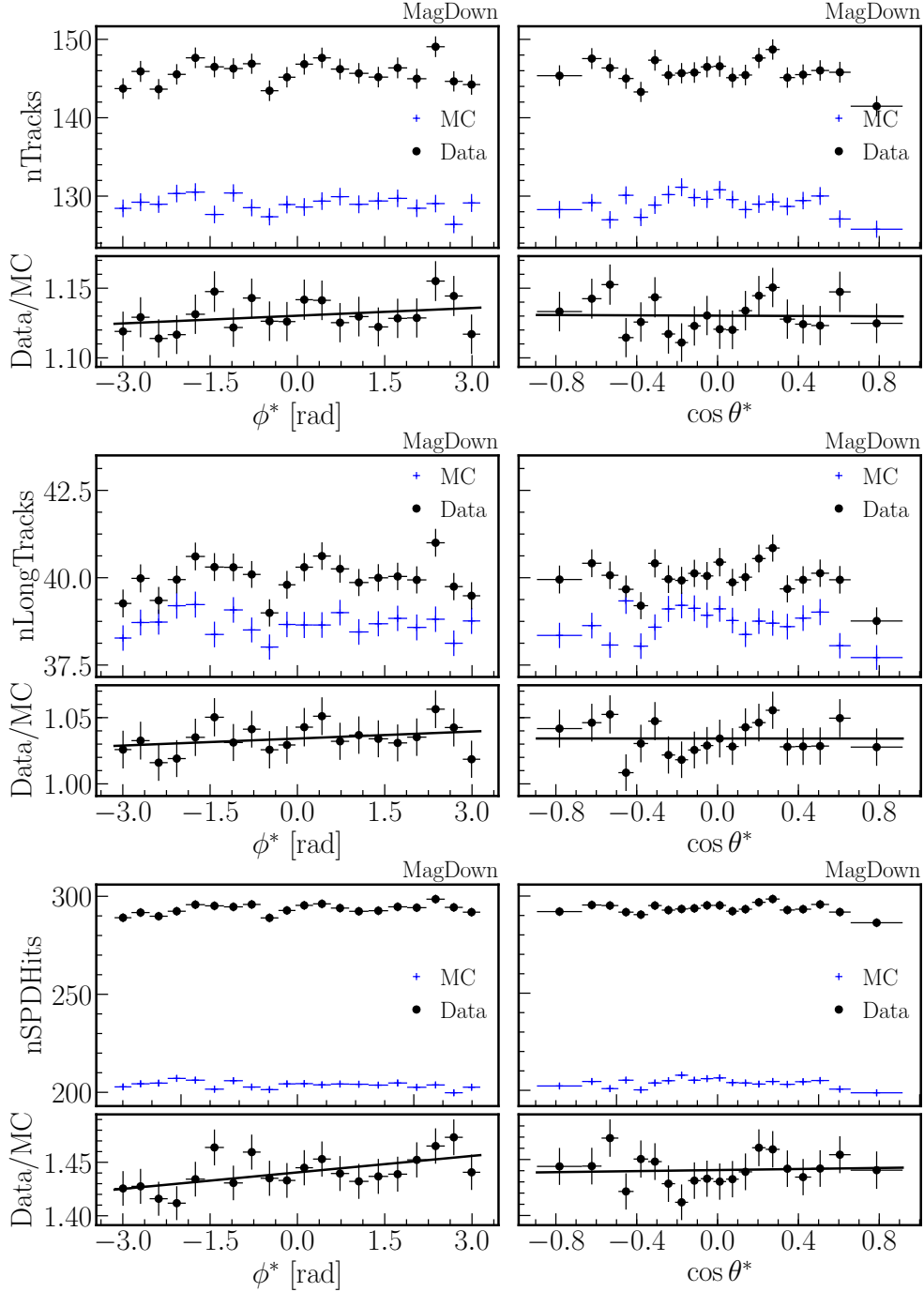
Figure A.2: The number of tracks (top), the number of long tracks (middle) and the number of hits in the scintillating pad detector (bottom) as a function of ϕ^* (left) and $\cos\theta^*$ (right) for negative magnet polarity only. Data is shown with black circles, MC with blue plusses. The lower panels show the data-to-MC ratios with the straight line fit. Error bars represent statistical uncertainties only.

A.3   2D residual plots
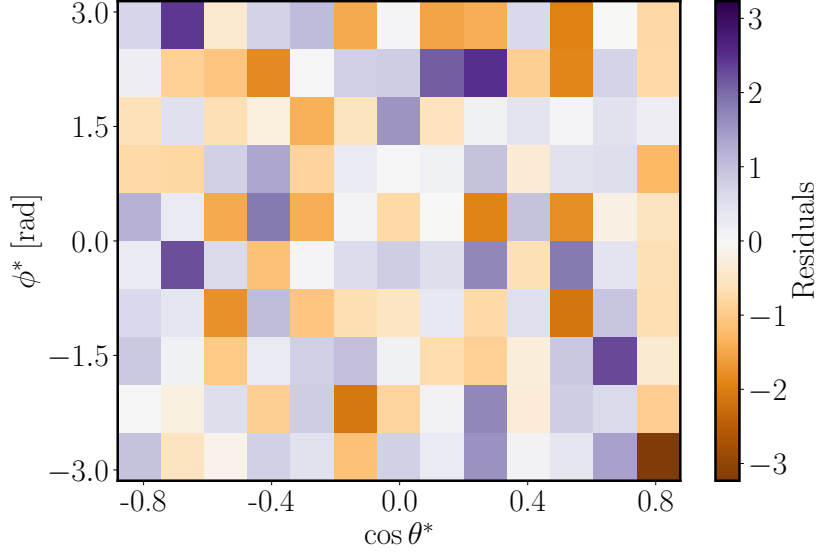
Figure A.3: Residuals of 2D angular distribution for $0 < p_{\mathrm{T}}^{\mathrm{Z}} < 10$ GeV/c. Data from both magnet polarities is combined. 71.5% of the uncertainties are within 1σ. Residuals are calculated only from statistical uncertainties.
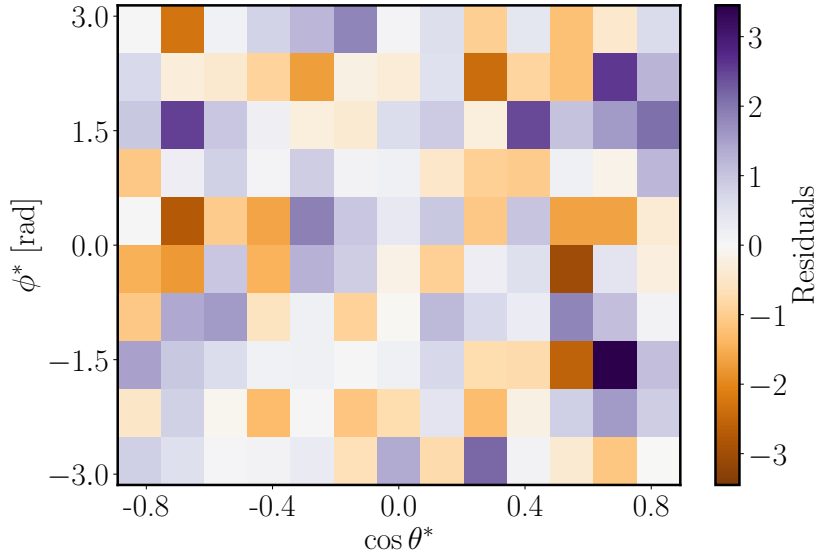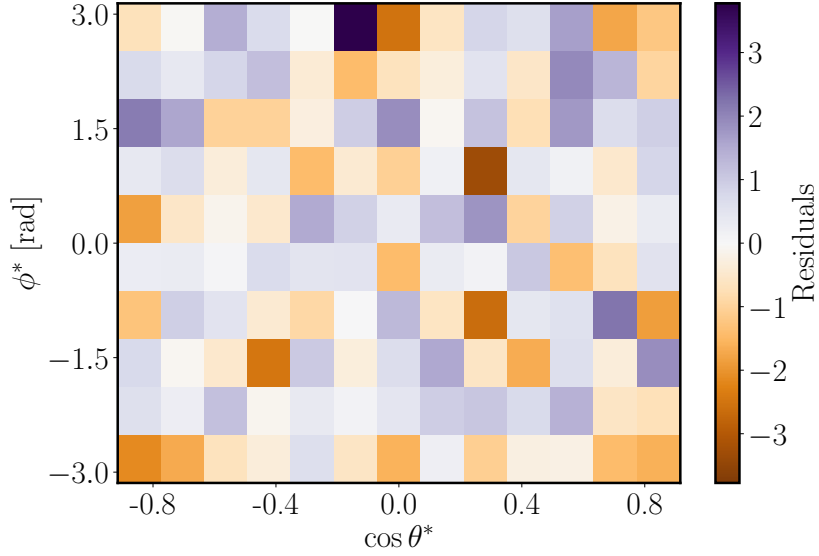

Figure A.4: Residuals of 2D angular distribution for $20 < p_{\mathrm{T}}^{\mathrm{Z}} < 30$ GeV/c. Data from both magnet polarities is combined. 64.6% of the uncertainties are within 1σ. Residuals are calculated only from statistical uncertainties.

Figure A.5: Residuals of 2D angular distribution for $p_T^Z > 30$ GeV/c. Data from both magnet polarities is combined. 64.6% of the uncertainties are within 1σ. Residuals are calculated only from statistical uncertainties.
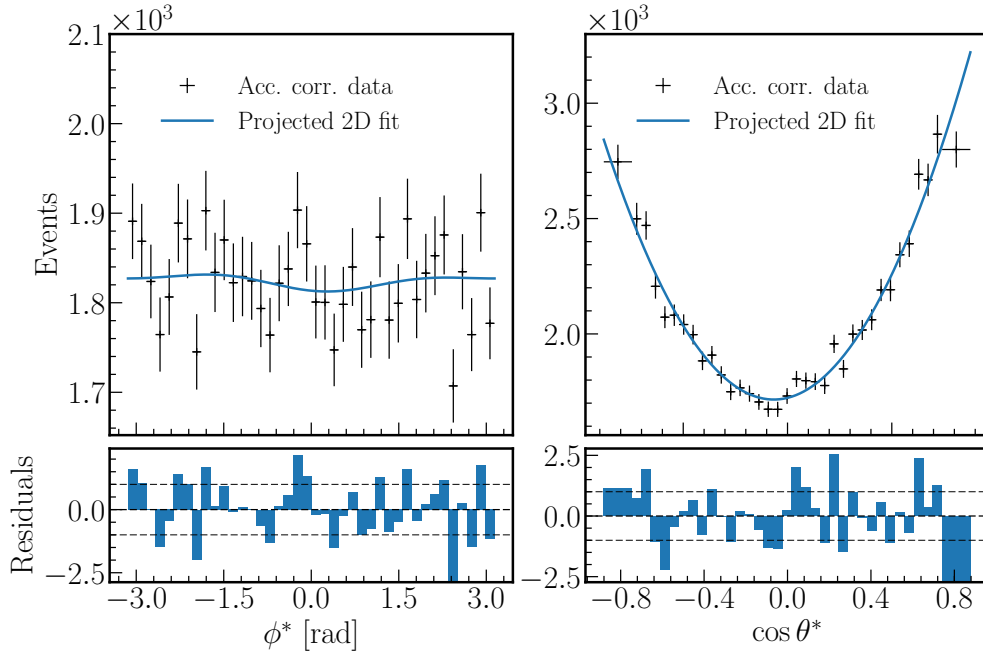
A.4   Projections of 2D fits

Figure A.6: Projections of 2D fit (blue line) to acceptance corrected data (black plusses) for ϕ^* (left) and $\cos\theta^*$ (right) for $0 < p_T^Z < 10$ GeV/c. Error bars show statistical uncertainties only. The lower panels show the residuals. 57.5% (ϕ^*) and 51.4% ($\cos\theta^*$) of the uncertainties are within 1σ.
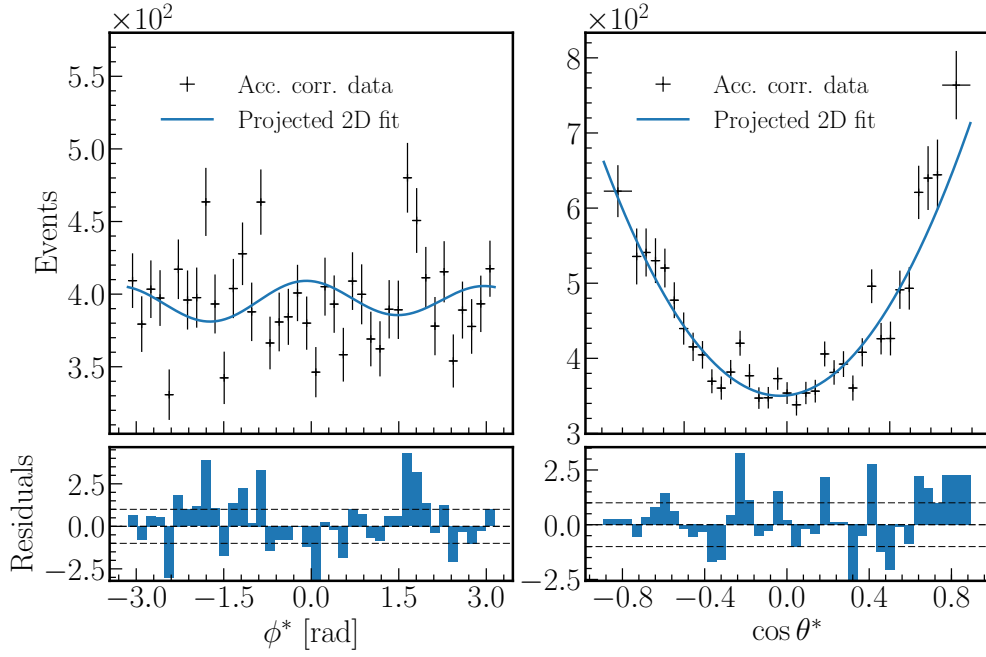
Figure A.7: Projections of 2D fit (blue line) to acceptance corrected data (black plusses) for ϕ^* (left) and $\cos\theta^*$ (right) $20 < p_T^Z < 30$ GeV/c. Error bars show statistical uncertainties only. The lower panels show the residuals. 50.0% (ϕ^*) and 57.1% ($\cos\theta^*$) of the uncertainties are within 1σ.
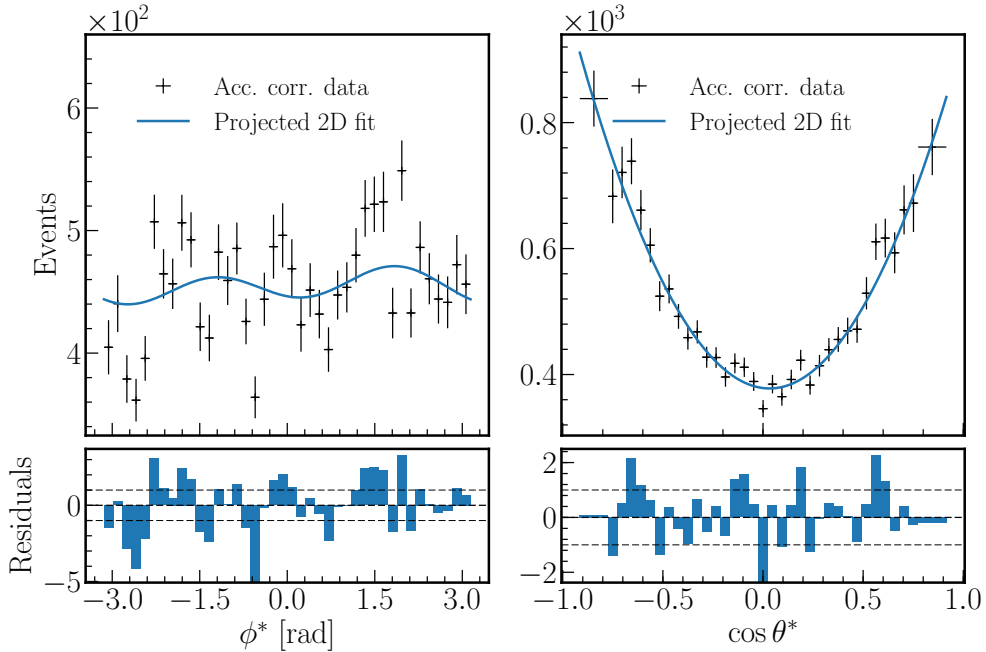

Figure A.8: Projections of 2D fit (blue line) to acceptance corrected data (black plusses) for ϕ^* (left) and $\cos\theta^*$ (right) for $p_T^Z > 30$ GeV/c. Error bars show statistical uncertainties only. The lower panels show the residuals. 35.0% (ϕ^*) and 65.7% ($\cos\theta^*$) of the uncertainties are within 1σ.
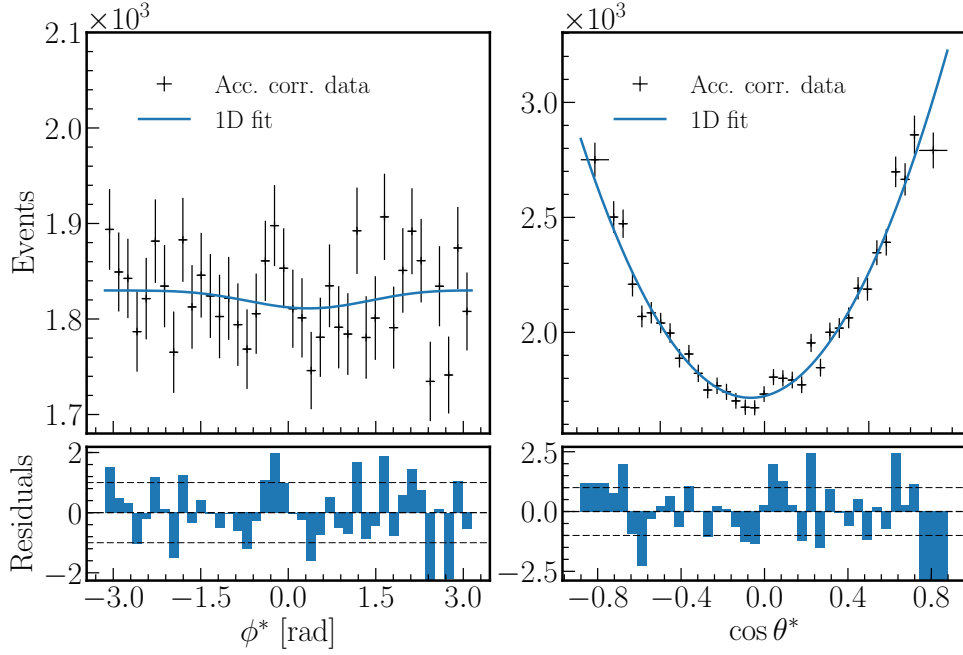
A.5   1D fits

Figure A.9: 1D fit (blue line) to acceptance corrected data (black plusses) for ϕ^* (left) and $\cos\theta^*$ (right) for $0 < p_T^Z < 10$ GeV/c. Error bars show statistical uncertainties only. The lower panels show the residuals. 62.5% (ϕ^*) and 54.3% ($\cos\theta^*$) of the uncertainties are within 1σ.
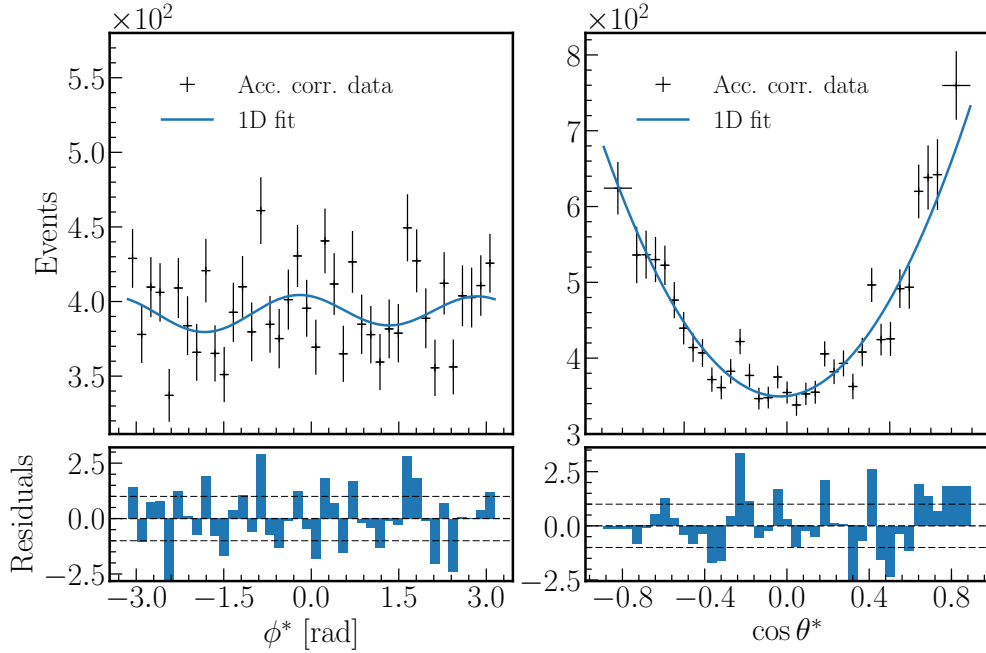

Figure A.10: 1D fit (blue line) to acceptance corrected data (black plusses) for ϕ^* (left) and $\cos\theta^*$ (right) for $20 < p_T^Z < 30$ GeV/c. Error bars show statistical uncertainties only. The lower panels show the residuals. 50.0% (ϕ^*) and 57.1% ($\cos\theta^*$) of the uncertainties are within 1σ.
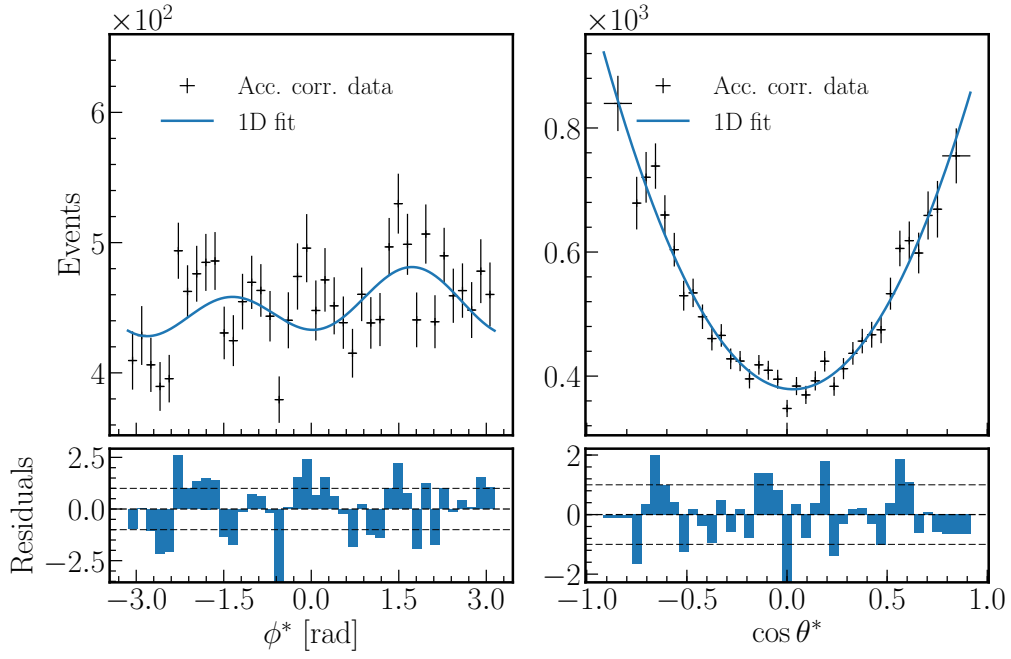
Figure A.11: 1D fit (blue line) to acceptance corrected data (black plusses) for ϕ^* (left) and $\cos\theta^*$ (right) for $p_T^Z > 30$ GeV/c. Error bars show statistical uncertainties only. The lower panels show the residuals. 45.0% (ϕ^*) and 65.7% ($\cos\theta^*$) of the uncertainties are within 1σ.

References

[1] C. Patrignani *et al.* [Particle Data Group], *Review of Particle Physics,* Chin. Phys. C **40** (2016) no.10, 100001. doi:10.1088/1674-1137/40/10/100001

[2] M. Thomson [Cambridge University Press], *Modern Particle Physics,* (2016)

[3] M. Tresch, *Tracking and Particle Identification at LHCb and Strange Hadron Production in Events with Z Boson,* 2017, CERN-THESIS-2017-107

[4] R. Gauld, A. Gehrmann-De Ridder, T. Gehrmann, E. W. N. Glover and A. Huss, *Precise predictions for the angular coefficients in Z-boson production at the LHC,* JHEP **1711** (2017) 003 doi:10.1007/JHEP11(2017)003 [arXiv:1708.00008 [hep-ph]].

[5] R. Sahoo, *Relativistic Kinematics*, arXiv:1604.02651 [nucl-ex].

[6] G. Aad *et al.* [ATLAS Collaboration], *Measurement of the angular coefficients in Z-boson events using electron and muon pairs from data taken at $\sqrt{s} = 8$ TeV with the ATLAS detector,* JHEP **1608** (2016) 159 doi:10.1007/JHEP08(2016)159 [arXiv:1606.00689 [hep-ex]].

[7] J. C. Collins and D. E. Soper, *Angular Distribution of Dileptons in High-Energy Hadron Collisions,* Phys. Rev. D **16** (1977) 2219. doi:10.1103/PhysRevD.16.2219

[8] D. Acosta *et al.* [CDF Collaboration], *Measurement of the polar-angle distribution of leptons from W boson decay as a function of the W transverse momentum in $p\bar{p}$ collisions at $\sqrt{s} = 1.8$ TeV,* Phys. Rev. D **70** (2004) 032004 doi:10.1103/PhysRevD.70.032004 [hep-ex/0311050].

[9] G. Steinbrück, *Measurement of the Angular Distribution of Electrons from W Boson Decays at D0,* doi:10.2172/1421493

[10] V. Khachatryan *et al.* [CMS Collaboration], *Angular coefficients of Z bosons produced in pp collisions at $\sqrt{s} = 8$ TeV and decaying to $\mu^+\mu^-$ as a function of transverse momentum and rapidity,* Phys. Lett. B **750** (2015) 154 doi:10.1016/j.physletb.2015.08.061 [arXiv:1504.03512 [hep-ex]].

[11] R. Aaij *et al.* [LHCb Collaboration], *LHCb Detector Performance,* Int. J. Mod. Phys. A **30** (2015) no.07, 1530022 doi:10.1142/S0217751X15300227 [arXiv:1412.6352 [hep-ex]].

[12] [LHCb Collaboration], *LHCb technical design report: Reoptimized detector design and performance*, CERN-LHCC-2003-030.

[13] R. Aaij *et al.* [LHCb Collaboration], *Measurement of charged particle multiplicities and densities in pp collisions at $\sqrt{s} = 7$ TeV in the forward region*, Eur. Phys. J. C **74** (2014) no.5, 2888 doi:10.1140/epjc/s10052-014-2888-1 [arXiv:1402.4430 [hep-ex]].

[14] A. A. Alves, Jr. *et al.* [LHCb Collaboration], *The LHCb Detector at the LHC*, JINST **3** (2008) S08005. doi:10.1088/1748-0221/3/08/S08005

[15] R. Aaij *et al.*, *The LHCb Trigger and its Performance in 2011,* JINST **8** (2013) P04022 doi:10.1088/1748-0221/8/04/P04022 [arXiv:1211.3055 [hep-ex]].

[16] M. Vesterinen [LHCb Collaboration], *Considerations on the LHCb dipole magnet polarity reversal* CERN-LHCb-PUB-2014-006

[17] T. Sjostrand, S. Mrenna and P. Z. Skands, *PYTHIA 6.4 Physics and Manual*, JHEP **0605** (2006) 026 doi:10.1088/1126-6708/2006/05/026 [hep-ph/0603175].

[18] R. Aaij *et al.* [LHCb Collaboration], *Measurement of forward W and Z boson production in pp collisions at* $\sqrt{s} = 8$ *TeV*, JHEP **1601** (2016) 155 doi:10.1007/JHEP01(2016)155 [arXiv:1511.08039 [hep-ex]].